

Fermi Large Area Telescope Bright Gamma-ray Source List

The *Fermi* LAT Collaboration

A. A. Abdo^{2,3}, M. Ackermann⁴, M. Ajello⁴, W. B. Atwood⁵, M. Axelsson^{6,7}, L. Baldini⁸, J. Ballet^{1,9}, D. L. Band^{10,11,12}, G. Barbiellini^{13,14}, D. Bastieri^{15,16}, M. Battelino^{6,17}, B. M. Baughman¹⁸, K. Bechtol⁴, R. Bellazzini⁸, B. Berenji⁴, G. F. Bignami¹⁹, R. D. Blandford⁴, E. D. Bloom⁴, E. Bonamente^{20,21}, A. W. Borgland⁴, A. Bouvier⁴, J. Bregeon⁸, A. Brez⁸, M. Brigida^{22,23}, P. Bruel²⁴, T. H. Burnett²⁵, G. A. Caliandro^{22,23}, R. A. Cameron⁴, P. A. Caraveo²⁶, J. M. Casandjian⁹, E. Cavazzuti²⁷, C. Cecchi^{20,21}, E. Charles⁴, A. Chekhtman^{3,28}, C. C. Cheung¹², J. Chiang⁴, S. Ciprini^{20,21}, R. Claus⁴, J. Cohen-Tanugi²⁹, L. R. Cominsky³⁰, J. Conrad^{6,17,31,32}, R. Corbet^{12,33}, L. Costamante⁴, S. Cutini²⁷, D. S. Davis^{12,33}, C. D. Dermer³, A. de Angelis³⁴, A. de Luca¹⁹, F. de Palma^{22,23}, S. W. Digel^{1,4}, M. Dormody⁵, E. do Couto e Silva⁴, P. S. Drell⁴, R. Dubois⁴, D. Dumora^{35,36}, C. Farnier²⁹, C. Favuzzi^{22,23}, S. J. Fegan²⁴, E. C. Ferrara¹², W. B. Focke⁴, M. Frailis³⁴, Y. Fukazawa³⁷, S. Funk⁴, P. Fusco^{22,23}, F. Gargano²³, D. Gasparrini²⁷, N. Gehrels^{12,38}, S. Germani^{20,21}, B. Giebels²⁴, N. Giglietto^{22,23}, P. Giommi²⁷, F. Giordano^{22,23}, T. Glanzman⁴, G. Godfrey⁴, I. A. Grenier^{1,9}, M.-H. Grondin^{35,36}, J. E. Grove³, L. Guillemot^{35,36}, S. Guiriec³⁹, Y. Hanabata³⁷, A. K. Harding¹², R. C. Hartman¹², M. Hayashida⁴, E. Hays¹², S. E. Healey⁴, D. Horan²⁴, R. E. Hughes¹⁸, G. Jóhannesson⁴, A. S. Johnson⁴, R. P. Johnson⁵, T. J. Johnson^{12,38}, W. N. Johnson³, T. Kamae⁴, H. Katagiri³⁷, J. Kataoka⁴⁰, N. Kawai^{41,42}, M. Kerr²⁵, J. Knödseder⁴³, D. Kocevski⁴, M. L. Kocian⁴, N. Komin^{9,29}, F. Kuehn¹⁸, M. Kuss⁸, J. Lande⁴, L. Latronico⁸, S.-H. Lee⁴, M. Lemoine-Goumard^{35,36}, F. Longo^{13,14}, F. Loparco^{22,23}, B. Lott^{35,36}, M. N. Lovellette³, P. Lubrano^{20,21}, G. M. Madejski⁴, A. Makeev^{3,28}, M. Marelli²⁶, M. N. Mazziotta²³, W. McConville^{12,38}, J. E. McEnery¹², S. McGlynn^{6,17}, C. Meurer^{6,31}, P. F. Michelson⁴, W. Mitthumsiri⁴, T. Mizuno³⁷, A. A. Moiseev^{10,38}, C. Monte^{22,23}, M. E. Monzani⁴, E. Moretti^{13,14}, A. Morselli⁴⁴, I. V. Moskalenko⁴, S. Murgia⁴, T. Nakamori⁴², P. L. Nolan⁴, J. P. Norris⁴⁵, E. Nuss²⁹, M. Ohno⁴⁶, T. Ohsugi³⁷, N. Omodei⁸, E. Orlando⁴⁷, J. F. Ormes⁴⁵, M. Ozaki⁴⁶, D. Paneque⁴, J. H. Panetta⁴, D. Parent^{35,36}, V. Pelassa²⁹, M. Pepe^{20,21}, M. Pesce-Rollins⁸, F. Piron²⁹, T. A. Porter⁵, L. Poupard⁹, S. Rainò^{22,23}, R. Rando^{15,16}, P. S. Ray³, M. Razzano⁸, N. Rea^{48,49}, A. Reimer⁴, O. Reimer⁴, T. Reposeur^{35,36}, S. Ritz¹², L. S. Rochester⁴, A. Y. Rodriguez⁴⁹, R. W. Romani⁴, M. Roth²⁵, F. Ryde^{6,17}, H. F.-W. Sadrozinski⁵, D. Sanchez²⁴, A. Sander¹⁸, P. M. Saz Parkinson⁵, J. D. Scargle⁵⁰, T. L. Schalk⁵, A. Sellerholm^{6,31}, C. Sgrò⁸, M. S. Shaw⁴, C. Shrader¹⁰, A. Sierpowska-Bartosik⁴⁹, E. J. Siskind⁵¹, D. A. Smith^{35,36}, P. D. Smith¹⁸, G. Spandre⁸,

P. Spinelli^{22,23}, J.-L. Starck⁹, T. E. Stephens^{50,52}, M. S. Strickman³, A. W. Strong⁴⁷,
D. J. Suson⁵³, H. Tajima⁴, H. Takahashi³⁷, T. Takahashi⁴⁶, T. Tanaka⁴, J. B. Thayer⁴,
J. G. Thayer⁴, D. J. Thompson^{1,12}, L. Tibaldo^{15,16}, O. Tibolla⁵⁴, D. F. Torres^{49,55},
G. Tosti^{20,21}, A. Tramacere^{4,56}, Y. Uchiyama⁴, T. L. Usher⁴, A. Van Etten⁴, N. Vilchez⁴³,
V. Vitale^{44,57}, A. P. Waite⁴, E. Wallace²⁵, P. Wang⁴, K. Watters⁴, B. L. Winer¹⁸,
K. S. Wood³, T. Ylinen^{6,17,58}, M. Ziegler⁵

¹Corresponding authors: J. Ballet, jean.ballet@cea.fr; S. W. Digel, digel@stanford.edu; I. A. Grenier, isabelle.grenier@cea.fr; D. J. Thompson, David.J.Thompson@nasa.gov.

²National Research Council Research Associate

³Space Science Division, Naval Research Laboratory, Washington, DC 20375

⁴W. W. Hansen Experimental Physics Laboratory, Kavli Institute for Particle Astrophysics and Cosmology, Department of Physics and SLAC National Accelerator Laboratory, Stanford University, Stanford, CA 94305

⁵Santa Cruz Institute for Particle Physics, Department of Physics and Department of Astronomy and Astrophysics, University of California at Santa Cruz, Santa Cruz, CA 95064

⁶The Oskar Klein Centre for Cosmo Particle Physics, AlbaNova, SE-106 91 Stockholm, Sweden

⁷Department of Astronomy, Stockholm University, SE-106 91 Stockholm, Sweden

⁸Istituto Nazionale di Fisica Nucleare, Sezione di Pisa, I-56127 Pisa, Italy

⁹Laboratoire AIM, CEA-IRFU/CNRS/Université Paris Diderot, Service d’Astrophysique, CEA Saclay, 91191 Gif sur Yvette, France

¹⁰Center for Research and Exploration in Space Science and Technology (CRESST), NASA Goddard Space Flight Center, Greenbelt, MD 20771

¹¹Deceased

¹²NASA Goddard Space Flight Center, Greenbelt, MD 20771

¹³Istituto Nazionale di Fisica Nucleare, Sezione di Trieste, I-34127 Trieste, Italy

¹⁴Dipartimento di Fisica, Università di Trieste, I-34127 Trieste, Italy

¹⁵Istituto Nazionale di Fisica Nucleare, Sezione di Padova, I-35131 Padova, Italy

¹⁶Dipartimento di Fisica “G. Galilei”, Università di Padova, I-35131 Padova, Italy

¹⁷Department of Physics, Royal Institute of Technology (KTH), AlbaNova, SE-106 91 Stockholm, Sweden

¹⁸Department of Physics, Center for Cosmology and Astro-Particle Physics, The Ohio State University, Columbus, OH 43210

¹⁹Istituto Universitario di Studi Superiori (IUSS), I-27100 Pavia, Italy

²⁰Istituto Nazionale di Fisica Nucleare, Sezione di Perugia, I-06123 Perugia, Italy

²¹Dipartimento di Fisica, Università degli Studi di Perugia, I-06123 Perugia, Italy

²²Dipartimento di Fisica “M. Merlin” dell’Università e del Politecnico di Bari, I-70126 Bari, Italy

²³Istituto Nazionale di Fisica Nucleare, Sezione di Bari, 70126 Bari, Italy

²⁴Laboratoire Leprince-Ringuet, École polytechnique, CNRS/IN2P3, Palaiseau, France

²⁵Department of Physics, University of Washington, Seattle, WA 98195-1560

-
- ²⁶INAF-Istituto di Astrofisica Spaziale e Fisica Cosmica, I-20133 Milano, Italy
- ²⁷Agenzia Spaziale Italiana (ASI) Science Data Center, I-00044 Frascati (Roma), Italy
- ²⁸George Mason University, Fairfax, VA 22030
- ²⁹Laboratoire de Physique Théorique et Astroparticules, Université Montpellier 2, CNRS/IN2P3, Montpellier, France
- ³⁰Department of Physics and Astronomy, Sonoma State University, Rohnert Park, CA 94928-3609
- ³¹Department of Physics, Stockholm University, AlbaNova, SE-106 91 Stockholm, Sweden
- ³²Royal Swedish Academy of Sciences Research Fellow, funded by a grant from the K. A. Wallenberg Foundation
- ³³University of Maryland, Baltimore County, Baltimore, MD 21250
- ³⁴Dipartimento di Fisica, Università di Udine and Istituto Nazionale di Fisica Nucleare, Sezione di Trieste, Gruppo Collegato di Udine, I-33100 Udine, Italy
- ³⁵CNRS/IN2P3, Centre d'Études Nucléaires Bordeaux Gradignan, UMR 5797, Gradignan, 33175, France
- ³⁶Université de Bordeaux, Centre d'Études Nucléaires Bordeaux Gradignan, UMR 5797, Gradignan, 33175, France
- ³⁷Department of Physical Sciences, Hiroshima University, Higashi-Hiroshima, Hiroshima 739-8526, Japan
- ³⁸University of Maryland, College Park, MD 20742
- ³⁹University of Alabama in Huntsville, Huntsville, AL 35899
- ⁴⁰Waseda University, 1-104 Totsukamachi, Shinjuku-ku, Tokyo, 169-8050, Japan
- ⁴¹Cosmic Radiation Laboratory, Institute of Physical and Chemical Research (RIKEN), Wako, Saitama 351-0198, Japan
- ⁴²Department of Physics, Tokyo Institute of Technology, Meguro City, Tokyo 152-8551, Japan
- ⁴³Centre d'Étude Spatiale des Rayonnements, CNRS/UPS, BP 44346, F-30128 Toulouse Cedex 4, France
- ⁴⁴Istituto Nazionale di Fisica Nucleare, Sezione di Roma “Tor Vergata”, I-00133 Roma, Italy
- ⁴⁵Department of Physics and Astronomy, University of Denver, Denver, CO 80208
- ⁴⁶Institute of Space and Astronautical Science, JAXA, 3-1-1 Yoshinodai, Sagamihara, Kanagawa 229-8510, Japan
- ⁴⁷Max-Planck Institut für extraterrestrische Physik, 85748 Garching, Germany
- ⁴⁸Sterrenkundig Instituut “Anton Pannekoek”, 1098 SJ Amsterdam, Netherlands
- ⁴⁹Institut de Ciències de l'Espai (IEEC-CSIC), Campus UAB, 08193 Barcelona, Spain
- ⁵⁰Space Sciences Division, NASA Ames Research Center, Moffett Field, CA 94035-1000
- ⁵¹NYCB Real-Time Computing Inc., Lattingtown, NY 11560-1025

ABSTRACT

Following its launch in June 2008, the *Fermi Gamma-ray Space Telescope* (*Fermi*) began a sky survey in August. The Large Area Telescope (LAT) on *Fermi* in 3 months produced a deeper and better-resolved map of the γ -ray sky than any previous space mission. We present here initial results for energies above 100 MeV for the 205 most significant (statistical significance greater than $\sim 10\text{-}\sigma$) γ -ray sources in these data. These are the best-characterized and best-localized **point-like (i.e., spatially unresolved)** γ -ray sources in the early-mission data.

Subject headings: Gamma rays: observations — surveys — catalogs; Fermi Gamma-ray Space Telescope; PACS: 95.85.Pw, 98.70.Rz

1. Introduction

Collections of information about what can be seen in the sky range from simple lists to complex catalogs. For high-energy γ -rays (photon energies above 100 MeV), the first effort of this type was a COS-B source list (Hermsen et al. 1977), followed by the second COS-B catalog (Swanenburg et al. 1981). The Energetic Gamma Ray Experiment Telescope (EGRET) on the *Compton Gamma Ray Observatory* yielded several catalogs, culminating in the third EGRET Catalog (3EG; Hartman et al. 1999) and an alternate catalog, EGR (Casandjian & Grenier 2008), but also including a catalog of just the sources seen above 1 GeV (Lamb and Macomb, 1997). The AGILE telescope has recently released its first catalog (Pittori et al. 2009)¹. The rapidly-changing field of TeV γ -ray astronomy has a number of on-line catalogs, e.g., TeVCat², **a frequently-updated compilation of announced**

⁵²Universities Space Research Association (USRA), Columbia, MD 21044

⁵³Department of Chemistry and Physics, Purdue University Calumet, Hammond, IN 46323-2094

⁵⁴Max-Planck-Institut für Kernphysik, D-69029 Heidelberg, Germany

⁵⁵Institució Catalana de Recerca i Estudis Avançats (ICREA), Barcelona, Spain

⁵⁶Consorzio Interuniversitario per la Fisica Spaziale (CIFS), I-10133 Torino, Italy

⁵⁷Dipartimento di Fisica, Università di Roma “Tor Vergata”, I-00133 Roma, Italy

⁵⁸School of Pure and Applied Natural Sciences, University of Kalmar, SE-391 82 Kalmar, Sweden

¹See <http://www.asdc.asi.it/agilebrightcat/>

²<http://tevcat.uchicago.edu/>

TeV sources from ground-based observatories.

The *Fermi Gamma-ray Space Telescope (Fermi)* Large Area Telescope (LAT) is a successor to EGRET, with greatly improved sensitivity, **angular** resolution, and energy range. This paper presents a list of bright LAT sources that have statistical significances of $10\text{-}\sigma$ or higher, based on the first three months of survey data. Although the first official LAT catalog is planned for release after the first year of operations, **(after the LAT gamma-ray data themselves become publicly available)**³, **this early list of bright sources was released to enable multiwavelength studies by the broader community and to support proposal preparation for Cycle 2 of the Fermi Guest investigator program.**

The reader is cautioned to avoid generalizing from this sample of sources. Some particular features are:

- The source list is not a complete summary of sources seen by the LAT. Many additional sources are detected with lower confidence levels in the LAT data than are included here (Sect. 3.3);
- The source list is not flux limited and hence not uniform. Only sources above a $10\text{-}\sigma$ statistical significance are included, as described below. **Moreover**, owing to the strong energy dependence both of the angular resolution of the LAT and of the intensities of backgrounds, the limiting flux is dependent on spectral hardness. Because γ -ray sources are seen against a background of diffuse gamma radiation, which is highly non-uniform across the sky, e.g., (Hunter et al. 1997; Strong et al. 2004), the limiting flux for a given statistical significance **and spectral shape** varies with position (Sect. 3.3).
- The source list does not include detailed information about the energy spectra of individual sources.

Because this list is a step toward the first LAT catalog, we adopt the terminology for sources that will be used in that catalog, with a 0 prefix. The source designation is 0FGL JHHMM.m+DDMM where the 0 refers to the preliminary nature of this list and FGL represents *Fermi* Gamma-ray LAT (Sect. 5).

³See <http://fermi.gsfc.nasa.gov/ssc/proposals/>.

2. Gamma-ray Detection with the Large Area Telescope

The LAT is a pair-production telescope (Atwood et al. 2009). The tracking section has 36 layers of silicon microstrip detectors to record the tracks of charged particles, interleaved with 16 layers of tungsten foil (12 thin layers, 0.03 radiation length, at the top or front of the instrument, followed by 4 thick layers, 0.18 radiation length, in the back section) to promote γ -ray pair conversion. **Below the tracker lies** an array of CsI crystals to determine the γ -ray energy. The tracker is surrounded by segmented charged-particle **anticoincidence** detectors (plastic scintillators with photomultiplier tubes) to reject cosmic-ray backgrounds. The LAT’s improved sensitivity compared to EGRET stems from a large peak effective area ($\sim 8000 \text{ cm}^2$, or ~ 6 times greater than EGRET’s), large field of view ($\sim 2.4 \text{ sr}$, or nearly 5 times greater than EGRET’s), good background rejection, superior angular resolution (68% containment angle $\sim 0.6^\circ$ at 1 GeV for the front section and about a factor of 2 larger for the back section, **vs. $\sim 1.7^\circ$ at 1 GeV for EGRET; Thompson et al. 1993**), and improved observing efficiency (keeping the sky in the field of view with scanning observations, **vs. inertial pointing for EGRET**). Pre-launch predictions of the instrument performance are described in Atwood et al. (2009). Verification of the on-orbit response is in progress (**Abdo et al. 2009q**) but the indications are that it is close to expectations.

The data analyzed for this source list were obtained during 4 August 2008 - 30 October 2008 (LAT runs 239503624 through 247081608, where the numbers refer to the Mission Elapsed Time, **or MET**, in seconds since 00:00 UTC on 1 January 2001). During this time *Fermi* was operated in sky scanning survey mode (viewing direction rocking 35° north and south of the zenith on alternate orbits, except for a few hours of special calibration observations during which the rocking angle was much larger than nominal for survey mode or the configuration of the LAT was different from normal for science operations. Time intervals when the rocking angle was larger than 47° have been excluded from the analysis, because the bright limb of the Earth enters the field of view (see below). In addition, two short time intervals associated with gamma-ray bursts (GRB) that were detected in the LAT have been excluded. These intervals correspond to GRB 080916C (MET 243216749–243217979, (Abdo et al. 2009a)) and GRB 081024B (MET 246576157–246576187). The total live time included is 7.53 Ms, corresponding to 82% efficiency after accounting for readout dead time and for observing time lost to passages through the South Atlantic Anomaly ($\sim 13\%$).

The standard onboard filtering, event reconstruction, and classification were applied to the data (Atwood et al. 2009), and for this analysis the ‘Diffuse’ event class⁴ is used.

⁴See http://fermi.gsfc.nasa.gov/ssc/data/analysis/documentation/Cicerone/Cicerone_Data/LAT_DP.html.

This is the class with the least residual contamination from charged-particle backgrounds. The tradeoff for using this event class is primarily reduced effective area, especially below 500 MeV. Test analyses were made with the looser ‘Source’ class cuts and these were found to be less sensitive overall than Diffuse class for source detection and characterization.

The alignment of the *Fermi* observatory viewing direction with the z axis of the LAT was found to be stable during survey-mode observation (Abdo et al. 2009q). The instrument response functions – effective area, energy redistribution, and point-spread function (PSF) – used in the likelihood analyses described below were derived from **GEANT4**-based Monte Carlo simulations of the LAT using the event selections corresponding to the Diffuse event class. The Monte Carlo simulations themselves were calibrated prior to launch using accelerator tests of flight-spare ‘towers’ of the LAT (Atwood et al. 2009). Consistency checks with observations of bright sources in flight data are in progress (Abdo et al. 2009q). Early indications are that the effective area below 100 MeV was overestimated **by as much as 30% owing to pile-up effects in the detectors**. The source detection and spectral fitting analyses **described below use only data >200 MeV. The impact of the lower-than-predicted effective area below 200 MeV is limited. The Diffuse event class already had relatively little effective area below 200 MeV, and so the impact on sensitivity for source detection is small.** Analyses of flight data suggest that the PSF is somewhat broader than the calculated Diffuse class PSF at high energies; the primary effect for the current analysis is to decrease the localization capability somewhat.

For the bright source analysis a cut on zenith angle was applied to the Diffuse class events to limit the contamination from albedo γ -rays from interactions of cosmic rays with the upper atmosphere of the Earth. These interactions make the limb of the Earth (zenith angle $\sim 113^\circ$ at the 565 km, nearly-circular orbit of *Fermi*) an intensely-bright γ -ray source (Thompson et al. 1981). The limb is very far off axis in survey mode observations, but during a small fraction of the time range included in this analysis the rocking angle reached angles as great as 47° (see above) and so the limb was only $\sim 66^\circ$ off axis. Removing events at zenith angles greater than 105° affects the exposure calculation negligibly but reduces the overall background rate. After these cuts, the data set contains 2.8×10^6 γ -rays with energies >100 MeV.

Figures 1 and 2 summarize the data set used for this analysis. The **intensity** map of Figure 1 shows the dramatic increase at low Galactic latitudes of the brightness of the γ -ray sky. Figure 2 shows the corresponding exposure map for the representative energy 1 GeV. The average exposure is ~ 1 Ms and nonuniformities are relatively small (about 30% difference between minimum and maximum), with the deficit around the south celestial pole due to loss of exposure during passages of *Fermi* through the South Atlantic Anomaly

(Atwood et al. 2009).

3. Construction of the Bright Source List

Although Figure 1 shows some obvious bright sources, finding and measuring the properties of even the high-confidence sources involves more than visual inspection of the map. **Because this analysis involves the entire sky and the broad energy range of the LAT, it is necessarily more complex than the analysis of an individual source.**

The source list was built on the basis of the full time interval. That is, we did not attempt to detect potentially flaring sources on shorter time scales, although we did check for variability of the sources (Sect. 3.5) after the list was constructed. Three steps were applied in sequence: detection, localization, significance estimate. At each step only a subset of the list at the previous step was kept. In that scheme the bright source list threshold is defined at the last step, but the completeness is controlled by the first one. After the list was defined we determined the source characteristics (flux in two energy bands, time variability) and we searched for possible counterparts.

3.1. Detection

At this time we do not have a good way to look for sources directly in the 3D space of position and energy so we used standard image detection techniques on counts images integrated over energy, **in which each event is simply stacked into the pixel corresponding to its best-guess incident direction.** The algorithm we used (*mr_filter*) is based on wavelet analysis in the Poisson regime (Starck & Pierre 1998). It looks for local deviations from the background model, leaving the background normalization free. **We used the same background model defined in Sect. 3.3, but without any spectral correction.** It returns a map of significant features (above some threshold) on which we run a peak-finding algorithm, SExtractor (Bertin & Arnouts 1996), to end up with a list of sources. We also used for comparison another wavelet algorithm, (*PGWave*, Damiani et al. 1997; Ciprini et al. 2007), which differs in the detailed implementation and returns directly a list of sources. Pre-launch simulations have shown that the latter was somewhat more sensitive on a flat background (**i.e.**, at high Galactic latitudes) but did not work as well in the Galactic plane. At the $10\text{-}\sigma$ level, the two detection methods yield identical source lists.

An important decision was which energy bands to use when applying the detection algorithms. The most important instrumental characteristic in this respect is the point-

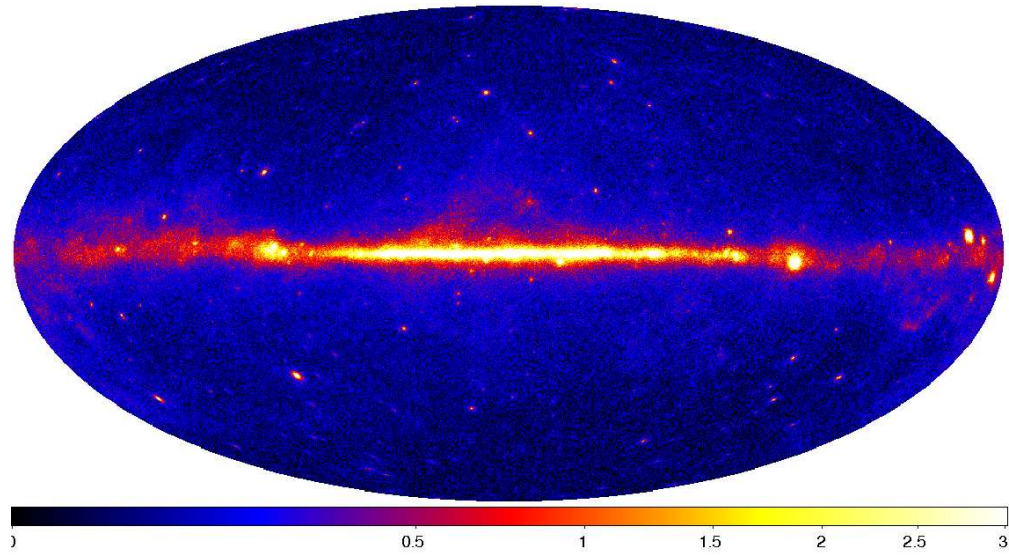


Fig. 1.— Sky map of the LAT data for the time range analyzed in this paper, Aitoff projection in Galactic coordinates. The image shows gamma-ray intensity for energies >300 MeV, in units of photons $\text{m}^{-2} \text{s}^{-1} \text{sr}^{-1}$.

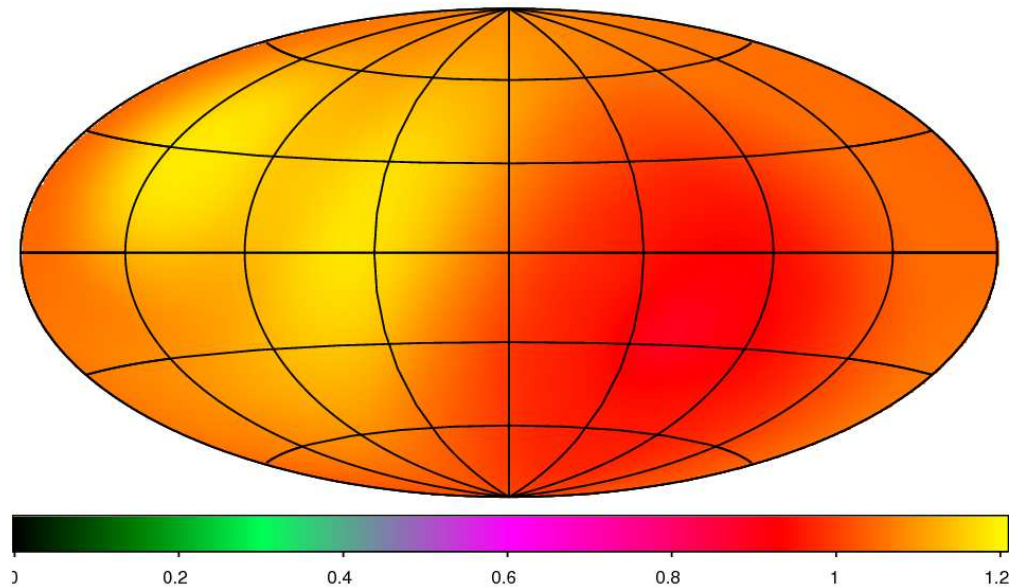


Fig. 2.— Exposure of the LAT for the time range analyzed in this paper, Aitoff projection in Galactic coordinates. The units are equivalent on-axis exposure in Ms.

spread function. The 68% containment radius improves by a factor of 25, from $\sim 5^\circ$ at 100 MeV to better than 1° at 1 GeV, reaching $\sim 0.2^\circ$ above 10 GeV (Atwood et al. 2009). For this reason there is (at least over 3 months) little confusion above 1 GeV and the diffuse background is not very limiting except in the Galactic ridge. On the other hand, most of the photons (83%) are recorded below 1 GeV. The majority of the sources in the Galactic plane have overlapping PSFs and are background dominated below 1 GeV (i.e., there are more background than source events inside the PSF). The starting energy therefore represents a trade between statistics and resolution.

Another important aspect is that the events converted in the top, thin layers of the tracker (*Front* events) have nearly a factor of two better PSF at a given energy than those converted in the bottom thick layers (*Back* events). **This corresponds to *Back* events of energy E having the same PSF width as *Front* events of energy $E/2$.** Therefore, to optimize the sensitivity of the source detection we **used separate** energy selections for *Front* and *Back* events.

The final scheme combines three energy bands. The full detection band (1.8×10^6 events) starts at 200 MeV for *Front* and 400 MeV for *Back* events. The remainder of the 2.8×10^6 events above 100 MeV carry little position information and were not used for source detection. We use a medium band starting at 1 GeV for *Front* and 2 GeV for *Back* events (3.2×10^5 events), which provides better position estimates for hard spectrum sources. We have also used a high energy band starting at 5 GeV for *Front* and 10 GeV for *Back* events. This band is very photon starved (3×10^4 events) but has essentially no background in a PSF-sized region and can be useful for very hard sources and to avoid confusion in the Galactic plane. We use smaller image pixels at high energy (0.1°) than in the medium band (0.2°) and the full energy band (0.3°) to adapt to the broader PSF at low energy. The bands are not exclusive (i.e., the full band includes the high energy photons) because the high-energy events always improve the detection. To obtain a global list of candidate sources we start with the sources detected in the high-energy band (best localization) and add the sources detected in the lower-energy bands in turn, excluding sources whose positions are consistent with detections at higher energies.

Because the source detection methods are standard algorithms not specific to *Fermi* they work in cartesian coordinates, not the spherical sky. We map the whole sky with 24 local World Coordinate System projections (Calabretta & Greisen 2002) in Galactic coordinates: 4 CAR (plate carrée) projections along the Galactic plane covering -10° to $+10^\circ$, 6 AIT(Hammer-Aitoff) projections on each side of the plane covering 10° to 45° , and 4 ARC (zenithal equidistant) projections (rotated 45° so that the pole is in a corner) covering 45° to 90° . Each map is 5° larger on each side than the area from which the sources are

extracted, to avoid border effects.

We set the threshold of the source detection step at 4σ . This resulted in 562 ‘seed’ sources. 290 were best detected in the full band, 212 in the medium band and 60 in the high band (among 151 total excesses above 4σ in that band).

3.2. Localization

The image-based detection algorithms provide estimates of the source positions, but the positions are not optimal because **the energy-dependent extent of the PSF is not fully taken into account**. These methods also do not supply error estimates on the positions.

The method that we use to localize the sources (*pointfit*) is a **binned** likelihood technique. It uses relatively narrow energy bins (typically 4 per decade) and sums $\log(\text{likelihood})$ over the energy bins. It does not use events below 500 MeV, which carry little information on position. To optimize the technique further the analysis gathers *Front* and *Back* events according to their PSF widths rather than their energies. Each source is treated independently. That means the model is a point source (with the same position but different width in each energy bin following the PSF) on top of a background model with free scaling in each energy bin. **The sources are treated in descending order** such that brighter sources are included in the background model for fainter ones. **The closest nearby source was 0.5° , with only a small effect on the fits to the lower energy bins.** The program returns the best-fit position and the error estimate (1σ along one dimension) based on the assumption that $-2\Delta\log(\text{likelihood})$ behaves as a χ^2 -distribution. **The LAT PSF itself is very close to axisymmetric (Atwood et al. 2009).** The error box is not in general circular due to fluctuations in the positions of the few high energy photons that dominate the localization precision. Here we neglect this effect, which is small for strong sources, and provide only error circles.

Of the 562 initial sources, *pointfit* did not converge for 50 at this step, or converged to another nearby source. **The reason could be confusion, or a soft spectrum leading to too few source events above 500 MeV.** We did not discard those outright, but kept their original positions. Several of them were deemed significant by the maximum likelihood algorithm (Sect. 3.3). We defined the positions and position uncertainties of those using a more precise but much slower tool (*gtfindsrc*) which accounts for all sources in the vicinity. **More precisely, we included in the local model all nearby sources (even those below the bright source limit defined in Sect. 3.3).** The spectral parameters of those within 1° of the current source were left free, but only the current source’s

position was adjusted in a given run. The same tool was used in a number of confused regions (mostly close to the Galactic plane) in which the primary analysis did not converge well. 32 sources in all were treated that way, including 13 of the bright sources presented here. In the end 532 sources survived the localization step.

The angular uncertainties for localization are determined from the shape of the likelihood function as described above. **This results in a 1-dimensional 1- σ error estimate Δx_{stat} . For a 2D axisymmetric gaussian distribution the 95% confidence level radius r_{95} is related to Δx_{stat} by a factor $\sqrt{-2\log(1-0.95)} = 2.45$. However examining the distribution of the position errors from high-confidence, identified sources, we found that we needed to increase the uncertainties by 40% in order to be sure of including 95% of the cases.**

For very bright sources like Vela, the observed offsets from the true position observed with the present analysis led us to add in quadrature an additional systematic uncertainty of 0.04 degrees to r_{95} .

$$r_{95}^2 = (1.4 \times 2.45 \times \Delta x_{\text{stat}})^2 + (0.04^\circ)^2 \quad (1)$$

Both the 1.4 correction factor and the 0.04° systematic uncertainty are conservative and are expected to improve.

Figure 3 illustrates the resulting position uncertainties as a function of the Test Statistic (TS) values obtained in Sect. 3.3. The relatively large dispersion that is seen at a given TS is in part due to the different local conditions (level of diffuse γ -ray emission) but primarily to the source spectrum. Hard sources are better localized than soft ones for the same TS because the PSF is so much narrower at high energy. At our threshold of $TS = 100$ (10- σ) the typical 95% uncertainty radius is about 10', and the maximum is 20'.

3.3. Significance and Thresholding

The detection and localization steps provide estimates of significance, but these are underestimates because the detection step does not explicitly use the energy information and the localization step does not use the low energy events. To better estimate the source significances we use a 3D maximum likelihood algorithm (*gtlike*) in unbinned mode **i.e.**, each event is considered individually **according to its direction, energy, and conversion location in the LAT**. This is part of the standard Science Tools software package⁵ currently at version 9r9. The *gtlike* tool provides for each source the best fit parameters and the Test

⁵<http://fermi.gsfc.nasa.gov/ssc/data/analysis/documentation/Cicerone/>

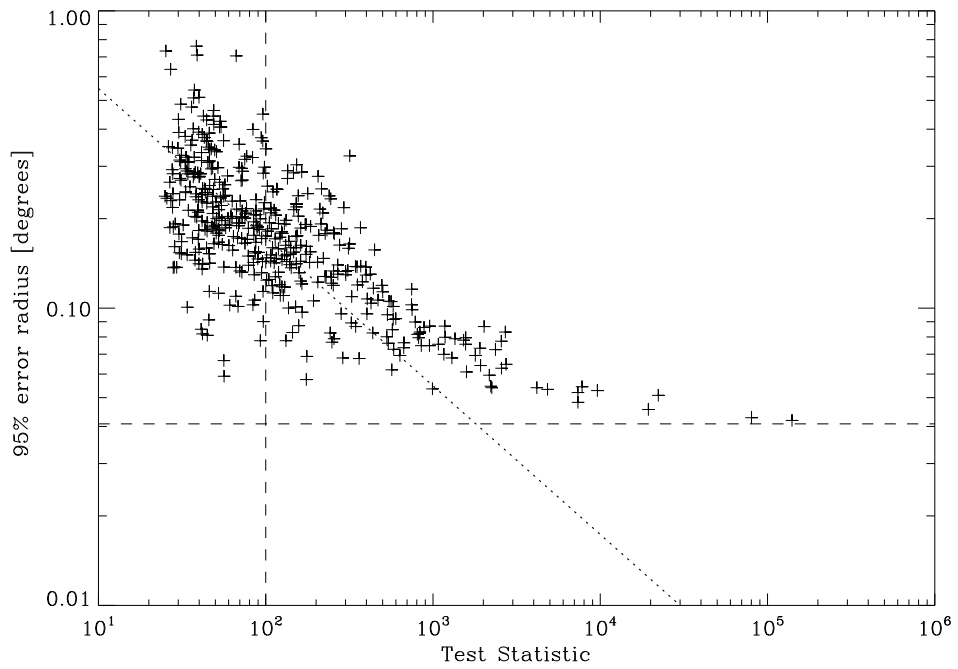


Fig. 3.— Source location uncertainty radii (r_{95} from Eq. 1) as a function of Test Statistic (Sect. 3.3), down to a limit of $TS = 25$. The dotted line is a $1/\sqrt{TS}$ trend for reference. The vertical dashed line is our $TS = 100$ threshold. The horizontal dashed line is the **absolute** systematic error that we adopted.

Statistic $TS = 2\Delta\log(\text{likelihood})$ between models with and without the source. That tool does not vary the source position, but it adjusts the source spectrum. It should be noted that *gtlike* does not include the energy dispersion in the TS calculation (**i.e., it assumes that the measured energy is the true energy**). Given the 8% to 10% $1\text{-}\sigma$ energy resolution of the LAT over the energy bands used in the present analyses, this approximation is justified. The underlying optimization engine is Minuit⁶. The code works well with up to ~ 30 free parameters, an important consideration for regions where sources are close enough together to partially overlap. Uncertainty estimates (and a full covariance matrix) are obtained from Minuit in the quadratic approximation around the best fit. For this stage we modeled the sources with simple power-law spectra.

The TS associated with each source is a measure of the source significance, or equivalently the probability that such an excess can be obtained from background fluctuations alone. The probability distribution in such a situation (source over background) is not precisely known (Protassov et al. 2002). However since we consider only positive fluctuations, and each fit involves two degrees of freedom (flux and spectral slope), the probability to get at least TS at a given position in the sky is close to $1/2$ of the χ^2 distribution with two degrees of freedom (Mattox et al. 1996), so that $TS = 25$ corresponds to 4.6σ (one sided). Pre-launch simulations have shown that this **approximation** is indeed true if the background model is close to the truth.

The diffuse background is of course very important since it represents around 90% of the events. We model the Galactic diffuse emission using GALPROP, described in Strong et al. (2004) and Strong (2007), which uses a realistic representation of cosmic-ray propagation in the Galaxy and the resulting γ -ray emission; it uses distributions of gas based on radioastronomical surveys, and the interstellar radiation field from an extensive modelling package. For this work, the GALPROP package has been updated to include recent H I and CO surveys, more accurate decomposition into Galactocentric rings, **as well as a new calculation of the interstellar radiation field for inverse Compton emission (Porter et al. 2008). For this work the fit of the model to the *Fermi* data was improved by an increase in the inverse Compton component, and a flatter cosmic-ray gradient in the outer Galaxy.** The particular GALPROP run designation for our model is 54_59varh7S.

Because the fitted fluxes and spectra of the sources can be very sensitive to even slight errors in the spectral shape of the diffuse emission we allow **the Galactic diffuse model** to be corrected (i.e., multiplied) locally by a power law in energy with free normalization and **spectral** slope. The slope varies between 0 and 0.15 (making it harder) in the Galactic

⁶<http://lcgapp.cern.ch/project/cls/work-packages/mathlibs/minuit/doc/doc.html>

plane and the normalization by $\pm 20\%$. The isotropic component of the diffuse emission **represents the** extragalactic and residual backgrounds (**instrumental + Earth albedo**). **It** is modeled by a simple power law. Its **spectral** slope was fixed to $E^{-2.25}$, the best fit value at high latitude, and its normalization was left free. **The three free parameters were separately adjusted in each Region of Interest (see below).**

For this significance analysis, we used only events with energies above 200 MeV, because the fits to the diffuse spectrum were systematically high below 200 MeV; the extrapolation of the high-energy spectrum overestimated the data, **possibly because of the acceptance bias described in Sect. 3.6**. We feared that including the low-energy points could bias the whole process. This energy cut changes little the TS estimates except for the very softest sources. The high energy limit for the analysis was set to 100 GeV. **There were fewer than 1000 events above 100 GeV, and at this point we do not have a single source that is bright enough to check our calibration above that limit.**

We split the sky into overlapping circular Regions of Interest (RoI), each typically 15° in radius. The source parameters are free in the central part of each RoI (**which is chosen** such that all free sources are well within the RoI even at low energy). We adjust the RoI size so that not more than 8 sources are free at a time. Adding 3 parameters for the diffuse model, the total number of free parameters in each RoI is 19 at most. We needed 128 RoIs to cover the 532 seed positions.

We proceed iteratively. **All RoIs are processed in parallel and a global current model is assembled after each step in which the best fit parameters for each source are taken from the RoI whose center is closest to the source. At each step the** parameters of the sources close to the borders are fixed to their **values in the global model at the end of** the previous step; they **all start at 0 flux at the first step (the starting point for the spectral slope is 2)**. Sources formally outside the RoI (but which can contribute at low energy due to the broad PSF) are included in the model as well. We iterate over 5 steps (the fits change very little after the fourth). At each step we remove sources with low TS **and refit**, raising the threshold up to 25 (approximately $5\text{-}\sigma$) at the last step. **We have checked via simulations that removing the faint sources has little impact on the bright sources, much less so than changing the diffuse model does (Sect. 3.6).**

This procedure left 444 sources, among which 205 have $TS > 100$. We chose not to include the lower-significance sources ($TS < 100$) in the bright source list for two reasons:

- The number of sources per Test Statistic interval normally decreases with **increasing** TS for any logN-logS close to Euclidean. This is not the case with our procedure (there

are fewer sources at $25 < TS < 30$ than at $35 < TS < 40$) particularly in the Galactic plane. This is a rather sure sign that we are missing sources at low flux, and more so in the Galactic plane. Given the relatively rough nature of the detection procedure (Sect. 3.1) this is not particularly surprising.

- Judging by the spatial and spectral residuals the Galactic diffuse model is still in need of improvement (see Sect. 3.6). This uncertainty makes us wary of claiming detections of sources not too far above the diffuse level.

On the other hand the sources at $TS > 100$ can be seen by eye on the images and we are confident they are all real. Note that all excesses formally above $TS = 25$ were included in the maximum likelihood adjustments (including those described in Sect. 3.4 and 3.5) to avoid transferring their fluxes to the more-significant sources.

Figure 4 shows the source flux needed to reach a $10\text{-}\sigma$ significance level at any point in the sky for the 3-month time interval considered in this analysis. This is based on a calculation using the Galactic diffuse and isotropic background models, the instrument response functions of the LAT, and the pointing history during the 3 months, and assuming an $E^{-2.2}$ spectrum, the average spectral shape of the sources. This should be viewed as an indication **only** because the detection threshold depends on the source spectrum. Although the nonuniform exposure affects this map somewhat, the dominant factor is the strong diffuse emission along the Galactic plane.

3.4. Flux Determination

The maximum likelihood method described in Sect. 3.3 provides good estimates of the source significances, but not very accurate estimates of the fluxes. This is because the spectra of most sources do not follow a single power law over that broad an energy range (more than two decades). Among the two most populous **classes**, the AGN often show a broken power-law spectrum and the pulsars an exponentially cut off **power law**. In both cases fitting a single power law over the entire range overshoots at low energy where most of the photons are, and therefore biases the fluxes high (**on the other hand the effect on the significance is low due to the broad PSF and high background at low energies**). An additional difficulty is that the fit over the entire range stopped at 200 MeV, whereas comparison with previous missions requires that we provide fluxes starting at 100 MeV. Extrapolating back to 100 MeV would have added another error.

To provide better estimates of the source fluxes, we have decided to split the range in two and define two independent bands from 100 MeV to 1 GeV and 1 GeV to 100 GeV. **The**

1 GeV limit is largely arbitrary but is a round number that happens to split the data into approximately equal contributions to the sources’ significance. The list of sources remains the same in the two bands of course. Each band is treated in the same way as the full band in Sect. 3.3. The power-law slopes are fitted independently in each band for each source. We discard the slopes here because they are not very precise (the low band is not very broad and there are not many events in the high band) and keep only the flux estimates. Even though the fit is not good near 100 MeV as mentioned in Sect. 3.3 (see also Sect. 3.6), including the data down to 100 MeV still provides a more reliable estimate of the flux than extrapolation for all sources which do not follow exactly a power law. The estimate from the sum of the two bands is on average within 30% of the flux obtained in the previous section, with excursions up to a factor 2. **We have also compared those estimates with a more precise spectral model for the three bright pulsars (Vela, Geminga and the Crab). The flux estimates are within 5% of each other.**

An additional difficulty that does not exist when considering the full data is that, because we wish to provide the fluxes in both bands for all sources, we must handle the case of sources that are not significant in one of the bands or where the flux is poorly determined due to large uncertainty in the spectrum. This situation occurs even for the high-confidence sources reported here: 9 have $TS < 25$ for the 100 MeV - 1 GeV band, and 2 have $TS < 10$ **in this band**. No high-confidence source has $TS < 25$ in the 1-100 GeV band. This difference reflects the fact that the current study (and the LAT in general) is more sensitive at high energy. For the sources with $TS < 10$ or poorly-measured flux values (where the nominal uncertainty is comparable to the flux itself), we replace the flux value from the likelihood analysis by a $2\text{-}\sigma$ upper limit ($2\Delta\log(\text{likelihood}) = 4$), indicating the upper limit by a 0 in the flux uncertainty column **of Table 6**.

3.5. Variability

For this paper we wanted to flag sources that are clearly variable. To that end we use the same energy range as in Sect. 3.3 (200 MeV to 100 GeV) to study variability. To avoid ending up with too large error bars in relatively short time intervals, we froze the spectral index of each source to the best fit over the full interval. Sources do vary in spectral shape as well as in flux, of course, but we do not aim at characterizing source variability here, just detecting it. It is very unlikely that a true variability in shape will be such that it will not show up in flux at all.

We split the full three-month interval into $N_{\text{int}} = 12$ intervals of a little more than one week. This preserves some statistical precision for the moderately bright sources we are

dealing with here, while being sensitive in the right time **scale** for flaring blazars. Because we do not expect the diffuse emission to vary, we freeze the spectral adjustment of the Galactic diffuse component to the local (in the same RoI) best fit over the full interval. We need to leave **the normalization of at least one diffuse component** free (just to adapt to the natural Poisson variations of the background). Because it was not obvious which one to freeze we decided to leave both (Galactic and isotropic) free in each interval. So in the end the fitting procedure is the same as in Sect. 3.3 except that all spectral shape parameters are frozen. The faint sources were left free (**even when not significant in the current interval**) as well as the bright ones.

As in Sect. 3.4 it often happens that a source is not significant in all intervals. To preserve the variability index (Eq. 2) we keep the best fit value and its estimated error even when the source is not significant. This does not work, however, when the best fit is very close to zero **because in that case the log(likelihood) as a function of flux is very asymmetric**. Whenever $TS < 1$ we compute the $1\text{-}\sigma$ upper limit and replace the error estimate with **the difference between that upper limit and the best fit. This is an estimate of the error on the positive side only. The best fit itself is retained.**

Figures 5 and 6 show the fluxes derived for the Vela and Geminga pulsars as a function of time. As the brightest persistent sources, Vela and Geminga provide a reference for non-variability. Based on these light curves, we estimate that the instrument and processing (event classification) are stable on time scales of weeks to 2% relative precision. To be conservative we have added in quadrature a fraction $f_{\text{rel}} = 3\%$ of the average flux F_{av} to the error estimates (**for each 1-week time interval**) used to compute the variability index.

Figure 7 shows the flux derived for the AO 0235+164 blazar as a function of time. In contrast to the steady pulsars, many of the blazars detected by the LAT show strong variability.

The variability index is defined as a simple χ^2 criterion:

$$V = \sum_i \frac{(F_i - F_{\text{av}})^2}{\sigma_i^2 + (f_{\text{rel}} F_{\text{av}})^2} \quad (2)$$

where i runs over the 12 intervals and σ_i is the statistical uncertainty in F_i . Since F_{av} is not known a priori, this parameter is expected, in the absence of variability, to follow a χ^2 distribution with 11 ($= N_{\text{int}} - 1$) degrees of freedom. We set the variability flag True whenever the probability of getting the value of V or more by chance is less than 1% (so that we expect 2 false positives over the sample of 205 sources). This corresponds to $V > 24.7$. This variability index is robust for the bright sources considered here, although for less-significant sources methods that handle upper limits will be needed.

Figure 8 shows the relative variability of the sources. It is defined from the excess variance on top of the statistical and systematic fluctuations:

$$\delta F/F = \sqrt{\frac{\sum_i (F_i - F_{\text{av}})^2}{(N_{\text{int}} - 1)F_{\text{av}}^2} - \frac{\sum_i \sigma_i^2}{N_{\text{int}}F_{\text{av}}^2} - f_{\text{rel}}^2} \quad (3)$$

The typical relative variability is 50%, with only a few strongly variable sources beyond $\delta F/F = 1$. The dotted lines show how the relative variability depends on the variability index as a function of TS , assuming that the relative precision on flux is the same for all sources (we get **a relative precision of 0.16 for the flux** on average at $TS=100$). **So this means that the criterion we use is not sensitive to relative variations smaller than 60% at $TS = 100$. That limit goes down to 20% as TS increases to 1000.** Note that because the relative precision on flux is not exactly the same for all sources the cutoff, **expressed in relative variability**, is not sharp. It is clear that we must be missing many variable AGN below $TS = 1000$.

66 bright sources (one third of the sample) are declared variable. This is far more than the 2 false positives expected, so most of them are truly variable. This level of variability is not particularly surprising, as blazars are known to be strongly variable on timescales of days to weeks. We emphasize that sources not flagged may also show variability at lower amplitude or different time scales than used for this test. We refer to these other sources as “non-variable” (on weekly time scales) rather than “steady.”

3.6. Limitations and Systematic Uncertainties

A limitation of this work is that we did not attempt to test for source extension. All sources are assumed to be point-like. This is true for all known source populations in the GeV range (see Sect. 4). On the other hand the TeV instruments have detected many extended sources in the Galactic plane, mostly pulsar wind nebulae and supernova remnants, (e.g., Funk 2005; Abdo et al. 2007). The current level of LAT exposure cannot address source extension at the level seen by the TeV telescopes.

We have addressed the issue of systematics for localization in Sect. 3.2. This section deals with the systematic uncertainties on flux estimates. **An obvious one is the power-law representation within each energy band. If one source had a very curved spectrum (like a spectral line) its flux estimate certainly would be inaccurate. Our experience with those sources for which more detailed studies have been made, though, is that the current estimates are fully acceptable. Beyond that, there are two main sources of systematics: the imperfect knowledge of the instrument so**

early into the mission, and the imperfect modeling of the diffuse emission.

The fluxes are calculated using pre-launch calibrations (designated P6_V1) based on Monte Carlo simulations and a beam test at CERN (Atwood et al. 2009). In flight, the presence of pile-up signals in the LAT tracker and calorimeter left by earlier particles was revealed in periodic trigger events. This effect leads to a reduction of the actual acceptance as compared to the pre-launch prediction, as fewer events pass the rejection cuts, most notably for photons below 300 MeV. The magnitude of this reduction is still under investigation, but the fluxes reported here may be lower than the true ones by as much as 35% below 1 GeV and 15% above 1 GeV. Because of the current uncertainty, no correction has been applied to the results; these effects are being assessed in detail, and will then be included in a reprocessing of the data. This uncertainty applies uniformly to all sources. Our relative errors (comparing one source to another or the same source as a function of time) are much smaller, as indicated in Sect. 3.5.

It is interesting to note that the flux above 100 MeV that the LAT finds for the three historical pulsars (Vela, Geminga and the Crab) is actually very close to that reported in the 3EG catalog (Hartman et al. 1999). Geminga and the Crab are within 1σ , and the LAT flux for Vela (9.15×10^{-6} ph cm $^{-2}$ s $^{-1}$) is 11% higher than that of EGRET. This implies that the bias may be on the low side of our estimate, unless EGRET also underestimated the source flux.

The diffuse emission is the other important source of uncertainties. Contrary to the former, it does not affect all sources equally. It is essentially negligible (i.e., smaller than the statistical errors) outside the Galactic plane ($|b| > 10^\circ$) where the diffuse emission is faint and varying on large angular scales. It is also not much of a worry in the high band (> 1 GeV) where the PSF is sharp enough that the bright sources dominate the background under the PSF. But it is a serious issue inside the Galactic plane ($|b| < 10^\circ$) in the low band (< 1 GeV) and particularly inside the Galactic ridge ($|l| < 60^\circ$) where the diffuse emission is strongest and very structured, following the molecular cloud distribution. It is not easy to assess precisely how large the uncertainty is, for lack of a proper reference. We have tried re-extracting the source fluxes assuming a very different diffuse model, and the results tend to show that the systematic uncertainty more or less follows the statistical one (i.e., it is larger for fainter sources) and is of the same order. We have not increased the errors accordingly, though, because this alternative model does not fit the data as well as the reference model where the differences in the source fluxes are largest.

The net result of these considerations is that we expect our high energy fluxes to be reasonably accurate, but the low energy fluxes are not as reliable and should be treated with particular caution in the Galactic ridge.

4. Source Association and Identification

Even with the superior angular resolution of LAT compared to previous-generation γ -ray telescopes, the source location accuracy is not good enough to draw firm conclusions based on positional coincidence in most cases. A typical LAT error circle contains multiple stars, galaxies, X-ray sources, infrared sources, and radio sources. Determination of the nature of a given LAT source must therefore rely on **more information than only simple location**. Two principles lead the search for counterparts:

- Variability is a powerful diagnostic, particularly considering that many γ -ray sources are known to be variable. Searches for periodic variability (such as rotational and orbital motion) offer opportunities for unique identifications. Determining variability correlated with that seen at other wavelengths is another approach.
- LAT γ -ray sources are necessarily nonthermal objects involving large energy transfers. Physical properties of any candidate counterpart must be consistent with generation of a significant luminosity of gamma radiation.

In this analysis, the LAT team makes a clear distinction between a source *identification* and an *association* with an object at another wavelength. A firm identification of a source is based on a timing characteristic such as a periodicity for a pulsar or binary or a variability correlated with observations at another wavelength in the case of a blazar. An association is made for a statistically-improbable positional coincidence of a plausible γ -ray-producing object with a LAT source.

4.1. Automated Source Associations

In anticipating the large number of γ -ray sources that will be detected by the LAT in the course of the mission, we implemented an automated source association pipeline that attempts to make quantified associations between LAT sources and potential counterparts. In its implementation for the Bright Gamma-Ray Source List the pipeline is almost exclusively based on positional coincidence, yet is driven by past knowledge about GeV source classes (pulsars and blazars) and physical expectations (**such as total luminosity and nonthermal emission implying particle acceleration**). Future implementations will also include figure-of-merit (FoM) approaches (Sowards-Emmerd et al. 2003) but these first require careful training on firmly identified source classes.

For each LAT source the probability of association with a source in the counterpart catalog is estimated using a Bayesian approach (e.g., de Ruiter et al. 1977; Sutherland & Saunders 1992) that considers the spatial match between LAT source and counterpart in light of the position uncertainty r_{95} and the chance coincidence probability as inferred from the local source density in the counterpart catalog. Specifically we calculate the posterior probability of association

$$P_{\text{post}} = \left(1 + \frac{1 - P_{\text{prior}}}{P_{\text{prior}}} \frac{\pi \rho r_{95}^2}{2.996} e^{\Delta} \right)^{-1} \quad (4)$$

where ρ is the local counterpart density, $\Delta = 2.996 \times r^2/r_{95}^2$, r is the angular separation between LAT source and catalog counterpart, and P_{prior} is the prior probability of association that we use here as a constant tuning parameter whose value is adjusted for each counterpart catalog to give an approximately constant false association rate among the catalogs considered. Since the value of P_{post} depends on the choice of P_{prior} we arbitrary define a counterpart as a possible association if $P_{\text{post}} \geq 0.5$. We applied our pipeline to random realizations of plausible LAT catalogs ⁷ in order to find for each counterpart catalog the value of P_{prior} that does not produce more than a single spurious association.

Table 1 summarizes the catalogs that have been used in our automatic association procedure. We also quote the prior probabilities that have been employed and give the total number of objects in each catalog. Note that we make an exception to our procedure when we cross-correlate the EGRET 3EG and EGR and AGILE AGL catalogs with the LAT sources. Since in these cases the uncertainties in the localization of the counterparts is worse than for the LAT sources we consider all EGRET and AGILE sources as possible counterparts if the LAT and counterpart separation is less than the quadratic sum of their 95% confidence error radii.

The pulsar catalog (the ATNF Pulsar Catalogue, Manchester et al. 2005) is special in that we split it into high and low \dot{E}/d^2 sub-samples, where \dot{E} is the rate of energy loss of the pulsar and d is the distance. High \dot{E}/d^2 has been proposed as a good estimator of a pulsar’s γ -ray visibility (Smith et al. 2008), and downselecting the catalog to the 100 best candidates allows for a relatively large prior probability without inflating the number of false positives. For the remaining pulsars **our Monte Carlo simulations required a much smaller prior probability** (to keep the chance coincidences low) at the expense of reducing

⁷ The plausible LAT catalogs contained 1000 sources of which 75% were distributed isotropically over the sky and 25% were distributed along the Galactic plane following a 2D Gaussian shaped density profile with $\sigma = 40$ deg in longitude and $\sigma = 2$ deg in latitude. For each source an error radius r_{95} of 0.2 deg has been assumed.

Table 1: Catalogs used for automatic source association. For clarity the table has been divided into Galactic, extragalactic and γ -ray source catalogs.

Name	Objects	P_{prior}	Selection	Reference
Pulsars (high \dot{E}/d^2)	100	0.29	$\dot{E}/d^2 > 5 \cdot 10^{33} \text{ erg cm}^{-2} \text{ s}^{-1}$	Manchester et al. (2005)
Pulsars (low \dot{E}/d^2)	1527	0.044	$\dot{E}/d^2 \leq 5 \cdot 10^{33} \text{ erg cm}^{-2} \text{ s}^{-1}$	Manchester et al. (2005)
PWN	69	0.5		Roberts (2005) ^a
SNR	265	0.033		Green (2006) ^b
HMXB	114	0.17		Liu et al. (2006)
LMXB	187	0.19		Liu et al. (2007)
Microquasars	15	0.5		Paredes (2006)
Globular clusters	147	0.5		Harris (1997)
Blazars (CGRABS)	1625	0.14		Healey et al. (2008)
Blazars (BZCAT)	2686	0.043		Massaro et al. (2009)
Flat Spectrum Radio Sources (CRATES)	10272	0.022		Healey et al. (2007)
3EG catalog	271	n.a.		Hartman et al. (1999)
EGR	189	n.a.		Casandjian & Grenier (2008)
AGL	40	n.a.		Pittori et al. (2009)

^a<http://www.physics.mcgill.ca/pulsar/pwncat.html>

^b<http://www.mrao.cam.ac.uk/surveys/snrs/>

the number of potential associations. This procedure can be considered as a simple binary figure-of-merit approach which favours revealing high \dot{E}/d^2 counterparts of LAT sources.

The performance of our association scheme is illustrated in Figure 9, which shows the distribution of normalized angular separations between LAT sources and counterparts; the normalization is done with respect to the measured localization uncertainty (Sect. 3.2). We also show the expected distribution for the case that all sources have been correctly associated (dotted line) or are spurious associations (dashed line). Obviously, the observed distribution clearly follows the first trend, suggesting that most of our associations are indeed reasonable and that our efforts to reduce the number of false positives were successful. We notice that the histogram shows a slight trend to smaller angular separations than expected, which might result from a slight overestimation of our source localization uncertainties.

4.2. Alternate Associations, Firm Identifications, and Special Cases

4.2.1. Active Galactic Nuclei (AGN)

Active Galactic Nuclei have been recognized since the EGRET era as a well-defined class of gamma-ray sources. For this reason, we have adopted an alternate method of finding AGN associations beyond the automated association procedure described in the previous section. This method uses a Figure of Merit (FoM) approach similar to the one described by Healey et al. (2008), based not only on positional proximity but also on radio spectral index, X-ray flux, and radio flux (Abdo et al. 2009c). Details of this association procedure, including the calculated probabilities from **both the FoM and automated association approaches, can be found in that paper. Although most of the associations are found by both methods, about 11% are found only by one of the two. In order to maintain consistency with the LAT AGN paper (Abdo et al. 2009c), we show any association found by either method.**

It should be emphasized, however, that Abdo et al. (2009c) chose to apply the AGN analysis only to parts of the sky with Galactic latitudes more than 10° from the plane in order to have a more uniform sample, while the present analysis covers the entire sky. AGN are seen by LAT at lower Galactic latitudes, because the Galaxy is largely transparent to γ -rays. Due to Galactic extinction and source confusion, AGN identification is more difficult at low latitudes. Some of the unassociated LAT sources in this part of the sky can be expected to have AGN counterparts in further analysis, which is beyond the scope of this paper.

4.2.2. Firm identifications

For this early source list from the LAT, we have taken the conservative view that association, even with high probability, is not equivalent to firm identification. Error circles are still large compared to source localization at longer wavelengths. We adopt the approach that firm identification for the 0FGL sources is limited to those for which variability can unambiguously establish the source.

Firm identifications of pulsars are based on seeing the pulsations in the γ -ray data with high confidence. Using several statistical tests, we require that the γ -ray distribution in pulsar phase be inconsistent with random at a probability level of 10^{-6} or smaller. Examples are the 6 pulsars confirmed from the EGRET era, the radio-quiet pulsar found in the CTA 1 supernova remnant (Abdo et al. 2008), PSR J0030+0451 (Abdo et al. 2009o), PSR J1028–5819 (Abdo et al. 2009f) and PSR J2021+3651 (Abdo et al. 2009n). In total

the 0FGL source list includes 30 firm pulsar identifications. One third of the sources within 10° of the Galactic Plane have now been identified with pulsars.

The HMXB system LSI +61 303 is firmly identified based on the observation of the orbital period of the binary system (Abdo et al. 2009j). A search for periodicity in the similar source LS5039 is still in progress.

Firm identifications of AGN depend on finding correlated multiwavelength activity. This work is ongoing.

4.2.3. *Special cases – Pulsar Wind Nebulae (PWNe) and Supernova Remnants (SNRs)*

SNRs and PWNe that are positionally correlated with LAT sources are not listed as individual associations in the main source list table. Statistical indications are that SNRs that were coincident with EGRET sources are significantly correlated with the 0FGL sources. However, the large number of pulsars detected by the LAT, including radio-quiet pulsars (e.g., Abdo et al. 2008), suggests that even a positional coincidence with an SNR of an age, distance, and environment plausible for a γ -ray source may be due to a γ -ray pulsar. Of the 0FGL sources positionally associated with PWNe or SNRs, approximately 40% have already been found to contain γ -ray pulsars. At the present level of sensitivity for the LAT-detected pulsars, only the Crab has shown evidence for off-pulse emission that can be attributed to a PWN or SNR. Until the possibility of pulsed emission for such sources can be ruled out, we are reluctant to make any claims about individual PWNe or SNRs as possible LAT detections. Effectively, the high rate of pulsar detections increases the burden of proof for PWN and SNR candidates, for example via studies of source extents.

Table 2 shows the 0FGL sources that are associated positionally with PWNe and SNRs, plus 4 pulsars that do not (yet) show evidence of γ -ray pulsation. Torres et al. (2003) considered several of the SNRs in Table 2 in terms of their potential to be γ -ray counterparts to unidentified low-latitude EGRET sources. In the case of SNR G284.3–1.8 they argued that PSR J1013–5915 was more probably the γ -ray source.

5. The Source List

The bright source list is presented as a single table (Table 6). Table 3 is a description of the columns in Table 6. Within the table, sources that have firm identifications or tentative associations are listed by class. Table 4 describes those classes. Figure 10 shows the locations of the 205 bright sources, in Galactic coordinates. All associations with specific source classes

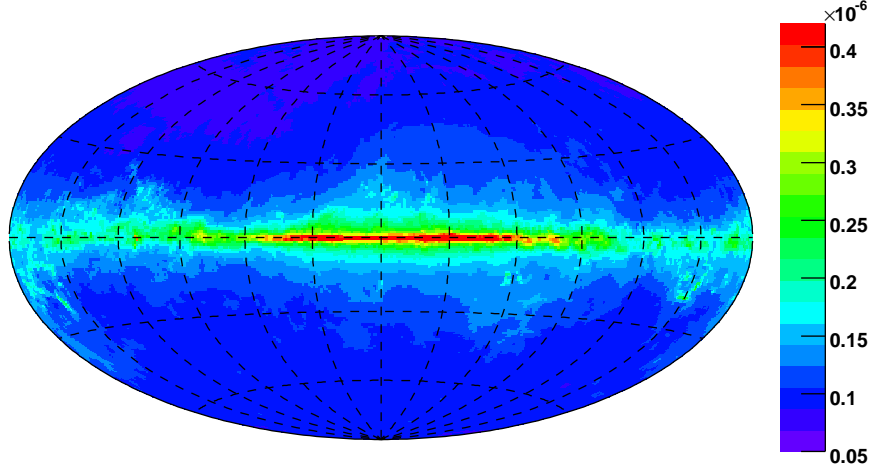


Fig. 4.— Flux ($E > 100$ MeV in $\text{ph cm}^{-2} \text{s}^{-1}$) needed for a $10\text{-}\sigma$ detection for the LAT data for the 3-month time range considered in this paper. The assumed photon spectral index is 2.2. Galactic coordinates.

Table 2. Potential Associations for Sources Near SNRs and PWNe

Name 0FGL	l	b	Assoc.
J0617.4+2234	189.08	3.07	SNR G189.1+3.0 (IC 443)
J1018.2–5858	284.30	–1.76	SNR G284.3–1.8 (MSH 10-53), PSR J1013–5915
J1106.4–6055	290.52	–0.60	SNR G290.1–0.8 (MSH 11-61A), PSR J1105–6107
J1615.6–5049	332.35	–0.01	SNR G332.4+0.1, PWN G332.5-0.28, PSR B1610-50
J1648.1–4606	339.47	–0.71	PSR J1648–4611
J1714.7–3827	348.52	0.10	SNR G348.5+0.1
J1801.6–2327	6.54	–0.31	SNR G6.4–0.1 (W28)
J1814.3–1739	13.05	–0.09	PWN G12.82–0.02
J1834.4–0841	23.27	–0.22	SNR G23.3–0.3 (W41)
J1855.9+0126	34.72	–0.35	SNR G34.7–0.4 (W44)
J1911.0+0905	43.25	–0.18	SNR G43.3–0.2
J1923.0+1411	49.13	–0.40	SNR G49.2–0.7 (W51)
J1954.4+2838	65.30	0.38	SNR G65.1+0.6

Note. — See text, Sect. 4.2.3. These sources are marked with a † in Table 6. They may be pulsars rather than the SNR or PWN named.

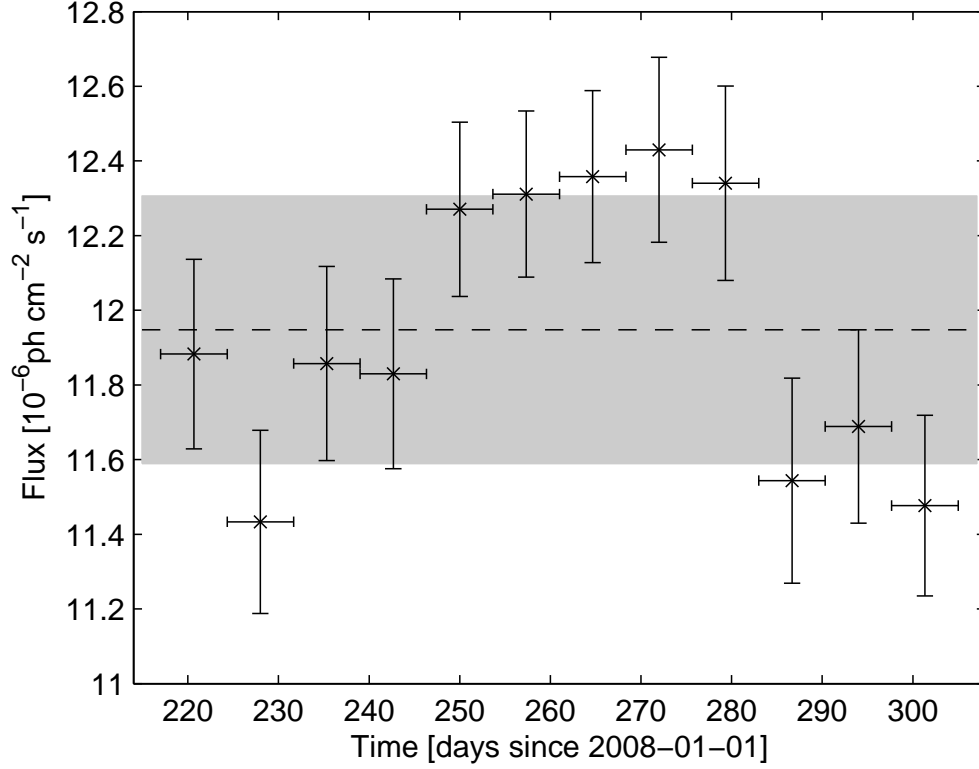


Fig. 5.— Light curve of Vela (0FGL J0835.4–4510) with fluxes from a single power-law fit and purely statistical error bars. Each interval is approximately one week. The dashed line is the average value. Because Vela is very bright it would **have been classified as variable using the statistical errors only**, but the flux dispersion is only **2.3% beyond statistical**. The grey area shows the 3% systematic error we have adopted. Note that because this analysis uses a power-law model over the entire range from 200 MeV to 100 GeV it grossly overestimates the true flux of Vela, but this effect does not depend on time.

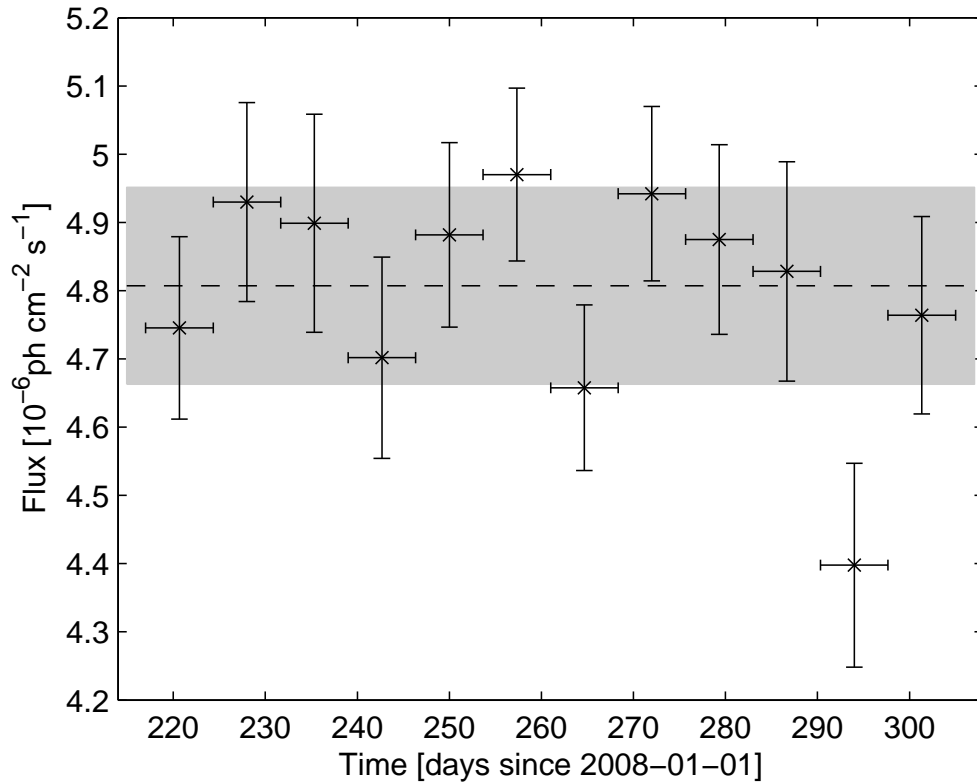


Fig. 6.— Same as Figure 5 for Geminga (0FGL J0634.0+1745). **That pulsar’s flux dispersion is 1.6% beyond statistical. Its variability index (Eq. 2) would not have exceeded the threshold even with pure statistical errors.**

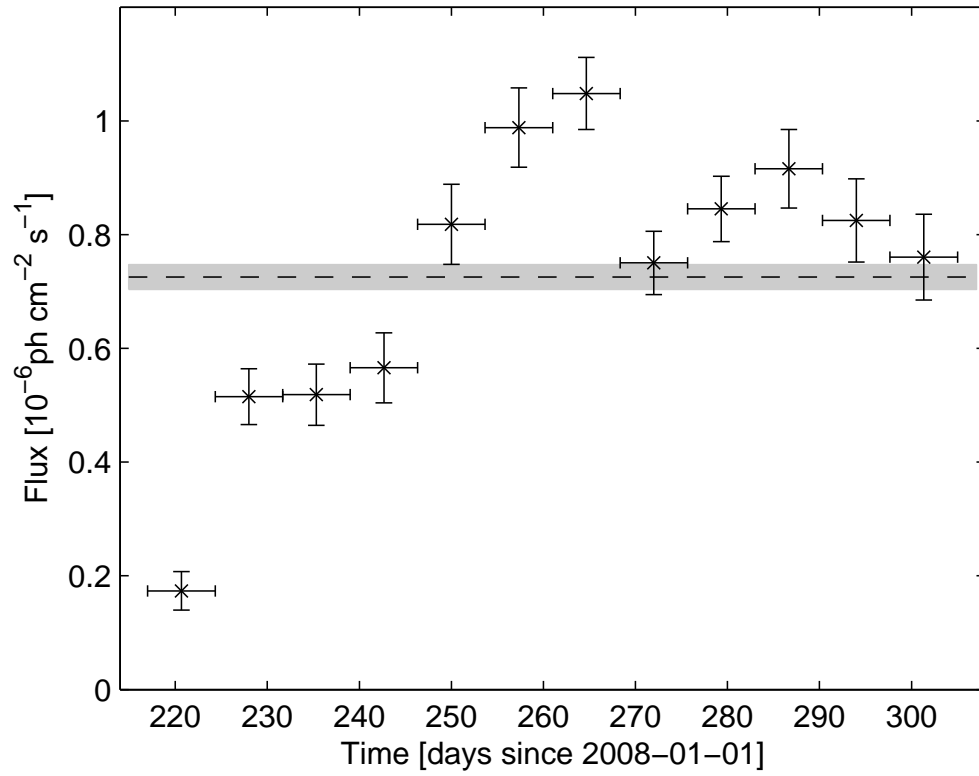


Fig. 7.— Same as Figure 5 for AO 0235+164 (0FGL J0238.6+1636), a variable blazar. Note the difference in scale from the Vela and Geminga light curves.

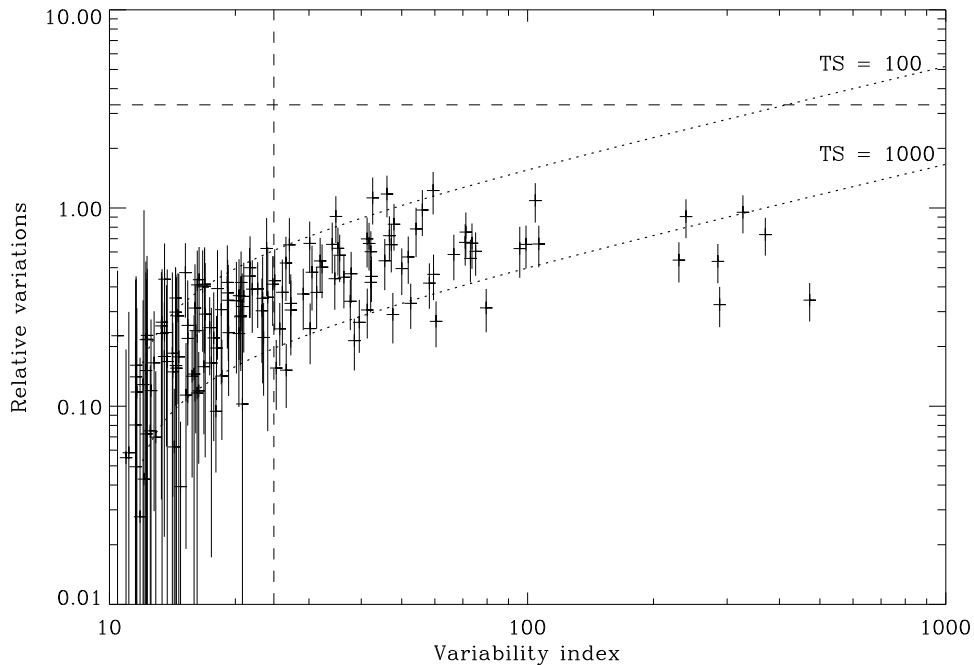


Fig. 8.— Relative source variability plotted as a function of the variability index (Eq. 3). The vertical dashed line shows where we set the variable source limit. The horizontal dashed line is the maximum relative variability that can be measured $\sqrt{N_{\text{int}} - 1}$. The dotted lines show how the variability index depends on $\delta F/F$ at our threshold ($TS = 100$) and for brighter sources ($TS = 1000$). At a given TS , the lower right part of the diagram is not accessible. **For more details see Sect. 3.5.**

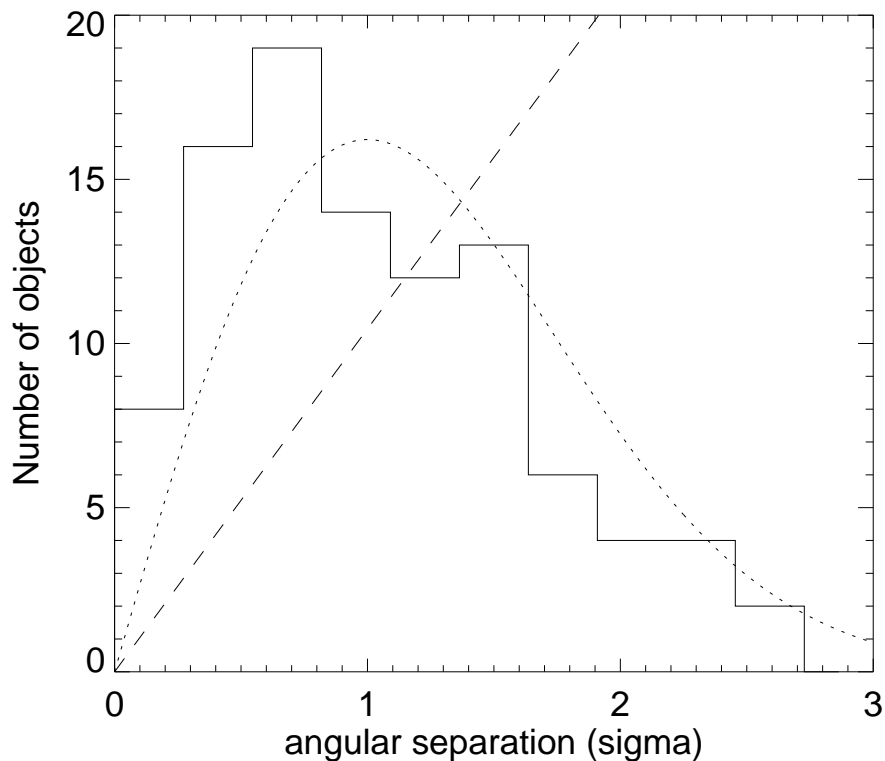


Fig. 9.— Distribution of angular separations between LAT sources and counterpart catalog associations expressed as $\sigma = 0.405 r/r_{95}$. The expected distribution in the case that all sources have been correctly associated is given as dotted line. **The peak at somewhat lower angular separation than the dotted prediction might indicate slightly better position determinations on average than (conservatively) assumed in this paper.** Conversely, the expected distribution in the case that all sources are spurious associations is given as the dashed line.

are also shown. Figure 11 is an enlargement of the bright source map, showing the region of the inner Galaxy. This list is available as a FITS file from the Fermi Science Support Center.

6. Discussion

As is clear from the references in this paper, much of the work on the early data from *Fermi* LAT is still in progress. In particular, we re-emphasize several caveats for use of this bright source list:

- Ongoing efforts to understand the calibration and improve the analysis techniques are underway. In many respects, therefore, the 0FGL source list is quite preliminary. Significant improvements are expected before the construction of the first full LAT catalog.
- The GALPROP diffuse model used in the analysis is still evolving. Matching the model to the large-scale emission is an iterative process. The diffuse model is particularly important for sources near the Galactic Plane.
- This source list is limited to high-confidence detections. It is not a full catalog.
- The 0FGL list information in two broad energy bands is not appropriate for detailed spectral modeling.
- This work is a “snapshot” of the LAT results covering only the **observation** time period August to October, 2008.
- The use of the diffuse class of events means that LAT has little sensitivity below 200 MeV for this particular analysis. As noted by Abdo et al. (2009c) in their analysis of AGN, the LAT is more sensitive to hard-spectrum sources than previous satellite instruments.

Despite these issues, the present work demonstrates the power of the LAT to make high-energy γ -ray observations and shows its potential for future discoveries. Although we feel it premature to draw far-reaching conclusions, some results stand out.

Table 3. LAT Bright Source List Description

Column	Description
Name	0FGL JHHMM.m+DDMM, constructed according to IAU Specifications for Nomenclature; m is decimal minutes of R.A.; in the name R.A. and Decl. are truncated at 0.1 decimal minutes and 1', respectively
R.A.	Right Ascension, J2000, deg, 3 decimal places
Decl.	Declination, J2000, deg, 3 decimal places
l	Galactic Longitude, deg, 3 decimal places
b	Galactic Latitude, deg, 3 decimal places
θ_{95}	Radius of 95% confidence region, deg, 3 decimal places
$TS^{1/2}$	Square root of likelihood TS from 200 MeV–100 GeV analysis, used for the $TS > 100$ cut, 1 decimal place
F_{23}	Flux 100 MeV–1 GeV (i.e., $\log_{10}E = 2-3$), $10^{-8} \text{ cm}^{-2} \text{ s}^{-1}$, 2 decimal places
ΔF_{23}	1- σ uncertainty on F_{23} , same units and precision. A 0 in this column indicates that the entry in the F_{23} flux column is an upper limit
$TS_{23}^{1/2}$	Square root of TS for the 100 MeV–1 GeV range, 1 decimal place
F_{35}	Flux for 1 GeV–100 GeV (i.e., $\log_{10}E = 3-5$), $10^{-8} \text{ cm}^{-2} \text{ s}^{-1}$, 2 decimal places
ΔF_{35}	1- σ uncertainty on F_{35} , same units and precision
$TS_{35}^{1/2}$	Square root of TS for the 1 GeV–100 GeV range, 1 decimal place
Var.	T indicates < 1% chance of being a steady source on a weekly time scale; see Sect. 3.5
γ -ray Assoc.	Identification or positional associations with 3EG, EGR, or AGILE sources
Class	Like 'ID' in 3EG catalog, but with more detail (see Table 4). Capital letters indicate firm identifications; lower-case letters indicate associations.
ID or Assoc.	Identification or positional associations with potential counterparts
Ref.	Reference to associated paper(s),

Table 4. LAT Bright Source List Source Classes

Class	Description
PSR	pulsar
pwn	pulsar wind nebula
hxb	high-mass X-ray binary (black hole or neutron star)
bzb	BL Lac type of blazar
bzq	FSRQ type of blazar
bzu	uncertain type of blazar
rdg	radio galaxy
glb	globular cluster
†	Special case - potential association with SNR or PWN (see Table 2)

Note. — Designations shown in capital letters are firm identifications; lower case letters indicate associations. In the case of AGN, many of the associations have high confidence (Abdo et al. 2009c). Among the pulsars, those with names beginning with LAT are newly discovered by the LAT.

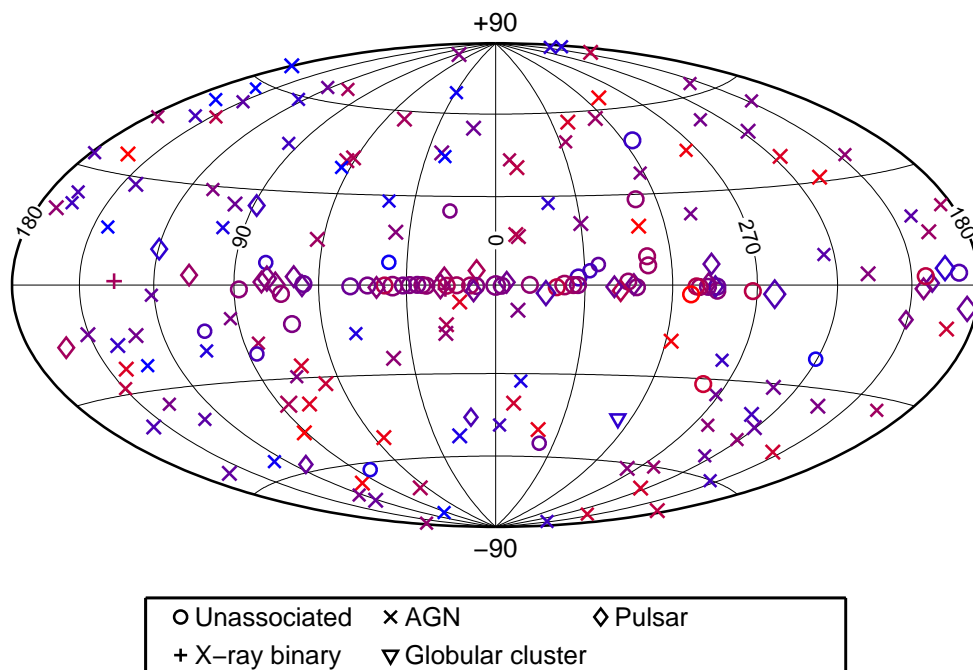


Fig. 10.— The LAT Bright Source List, showing the locations on the sky (Galactic coordinates in Aitoff projection) coded according to the legend. **Although quantitative spectral information is not presented, the colors of the symbols indicate relative spectral hardness on a sliding scale. Symbols more blue in color indicate sources with harder spectra than those that are more red.**

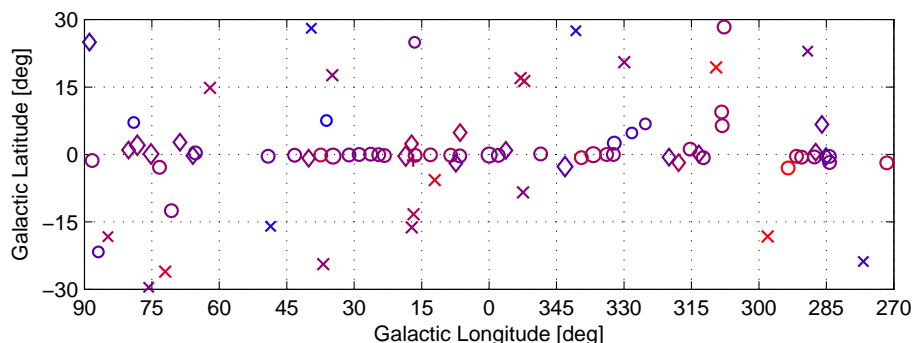


Fig. 11.— The LAT Bright Source List, showing the locations of sources in the inner Galaxy. The legend is the same as in Figure 10.

6.1. Characteristics of the 0FGL Sources

- Both Galactic and extragalactic populations are visible. 73 sources are found within 10° of the Galactic Plane, where they exhibit a characteristic concentration in the inner Galaxy; 132 are seen at higher Galactic latitudes.
- 66 of the bright LAT sources show solid evidence of variability **on weekly time scales during this three-month interval**. Figure 12 shows the locations of variable and non-variable sources, in Galactic Coordinates.
- The typical error radii for the sources (95% confidence) are less than $10'$.
- The Galactic latitude distribution of unassociated/unidentified γ -ray sources is very narrow (FWHM $<0.5^\circ$). If we assume a scale height for a Galactic population of 40 pc (Guibert et al. 1978), such a narrow latitude distribution points to a Galactic γ -ray source population with average distance in excess of $40/\sin 0.5^\circ$, namely 4.5 kpc.

6.2. Comparisons with Other High-Energy γ -ray Results

Before *Fermi*, the EGRET results represented the most complete view of the high-energy sky, but those results applied to the 1991-2000 era. In light of the variability seen in the EGRET γ -ray sources, significant differences were expected. A contemporaneous mission to *Fermi* is AGILE, which began operations over a year before *Fermi* and continues to operate. Here is a summary of comparisons with these missions:

- Of the 205 0FGL sources, 60 have nearby counterparts (the LAT source 95% uncertainty overlapping that of the EGRET source) found by the automated analysis in the 3EG catalog (271 sources); 43 in the EGR catalog (189 sources). Most of the sources seen by EGRET in the 1990s were not seen by LAT as bright sources in 2008. Approximately 40% of the bright LAT sources off the plane that have no former EGRET counterparts are found to be variable.
- **EGRET found few sources with flux less than 10×10^{-8} photons($E > 100$ MeV) $\text{cm}^{-2} \text{s}^{-1}$. A number of the 0FGL sources have fluxes well below this value (e.g., 0FGL J0033.6–1921). Such sources would not have been visible to EGRET.**
- Some sources, such as 0FGL J0428.7–3755, associated with blazar PKS 0426–380, have flux values well above the EGRET threshold but were not

seen by EGRET and yet are not noted as being variable in the 0FGL data. Such sources serve as a reminder that blazars are variable on many time scales, and the 0FGL sample covers only three months.

- Considering the highest-confidence sources, in its lifetime EGRET found 31 sources (in either the 3EG or EGR catalogs or both) with confidence level of $>10\text{-}\sigma$. The 0FGL list shows the dramatic improvement in sensitivity of the LAT.
- Five of the EGRET sources seen at $10\text{-}\sigma$ significance (all associated with flaring blazars: NRAO 190, NRAO 530, 1611+343, 1406–076, and 1622–297) do not appear in the LAT bright source list.
- 28 of the EGRET sources that have counterparts in the 0FGL list were previously listed as unidentified. Half of these, 14, have now been firmly identified in this early LAT analysis. 13 are pulsars; 1 is a HMXB.
- Of the 40 sources in the first AGILE catalog (which is contemporaneous but does not overlap in time with the 0FGL data), 32 are also found in the 0FGL list and 7 more, while not formally overlapping, are “near misses” to 0FGL sources. The one exception is AGL J1238+04, a source associated with a FSRQ. A LAT source consistent in position with this one is found at a lower significance during the first 3 months of operation, but the source has since flared (Tramacere & Rea 2009).

6.3. Some Results from the Association Analysis

Table 5 summarizes the census of associations in the Bright Source List. **The numbers of these associations that are considered firm identifications are shown in parentheses.**

- The AGN class (121 members) is the largest source type associated in the LAT data. Details of the analysis, together with the implications for AGN studies, are given by Abdo et al. (2009c). Two of the AGN found in this analysis are associated with radio galaxies; the rest are categorized as blazars. Note that 5 of the 0FGL AGN are not included in the Abdo et al. (2009c) analysis, because they are found within 10° of the Galactic Plane.
- Pulsars, including young radio pulsars, millisecond radio pulsars, and radio-quiet pulsars, form another well-defined class (30 members) in the LAT bright source list.

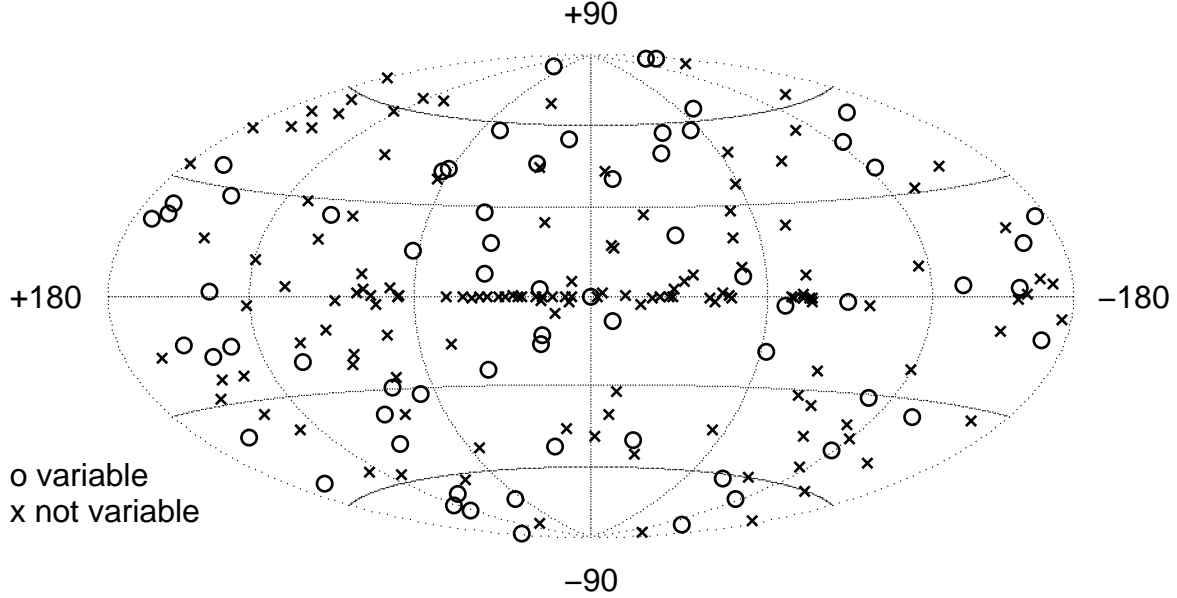


Fig. 12.— Locations of variable (*circles*) and non-variable (*crosses*) 0FGL sources, using the definition of variability in Sec. 3.5. The analysis is sensitive to variations on time scales of weeks to ~ 2 months..

Table 5. LAT Bright Source List Source Associations (Firm Identifications)

Class	Number
Radio/X-ray pulsar (PSR)	15 (15)
LAT gamma-ray pulsar (LAT PSR)	15 (15)
HMXB	2 (1)
BL LAC (bzb)	46 (0)
FSRQ (bzq)	64 (0)
Other blazar (Uncertain type, bzu)	9 (0)
Radio galaxy (rdg)	2 (0)
Globular Cluster (glb, see text)	1 (0)
LMC (see text)	1 (0)
† Special cases (see Table 2)	13 (0)
Unassociated	37 (0)

- Among the 0FGL sources, no associations were found with LMXB, starburst galaxies, prominent clusters of galaxies or Seyfert galaxies.
- 2 associations were found with HMXB sources, both of which are also seen at TeV energies: LSI +61 303 (Albert et al. 2008) and LS 5039 (Aharonian et al. 2006b). The association of 0FGL J0240.3+6113 with LSI +61 303 is considered a firm identification based on the orbital periodicity seen in the LAT emission (Abdo et al. 2009j). Analysis of LS 5039 is in progress.
- Globular cluster NGC 104 = 47 Tuc is associated with LAT source 0FGL J0025.1–7202; it should be emphasized that this globular cluster contains at least 23 millisecond radio pulsars and presumably contains many more as-yet undetected neutron stars.
- 0FGL J0538.4–6856 is seen in the direction of the Large Magellanic Cloud. The LMC X-ray pulsar associated with this source by the automated software (PSR J0537–6910) is one possibility. The source is also consistent with the direction of the 30 Doradus star-forming region. Work on this part of the sky is still in progress.
- 0FGL J0617.4+2234 lies within the projected direction of the shell of SNR IC443. A TeV source has also been seen close to the position of the LAT source. Detailed analysis of the LAT source is in progress.
- 0FGL J0910.2–5044, although visible in the summed map, was seen primarily as a Galactic transient in October, 2008 (Cheung et al. 2008).
- 0FGL J1746.0–2900 lies close to the Galactic Center. Modeling the diffuse emission in this general region is challenging. We consider any conclusions about the association of this source with the Galactic Center or other candidate γ -ray emitters in this region to be premature. The variability flag for this source is True, but the source is not extremely variable. This source barely met the criterion for being called variable. Work on this region is in progress.
- **37** of the 0FGL sources have no obvious counterparts at other wavelengths.

6.4. TeV Comparisons

Associations with TeV sources are based in this work only on positional correlation. Physical modeling or correlated variability would be needed in order to draw any conclusions from these associations. This is not an exhaustive list. We have omitted associations with

blazars, well-known objects such as the Crab Nebula, and sources discussed previously in the text.

- 0FGL J1024.0–5754 is spatially consistent with HESS J1023–575, itself not yet firmly identified, but noted for its possible connection to the young stellar cluster Westerlund 2 in the star-forming region RCW49 (Aharonian et al. 2007).
- 0FGL J1418.8–6058 is spatially coincident with HESS J1418–609 (Aharonian et al. 2006a), which may be the PWN powered by the LAT-discovered LAT PSR J1418–60.
- 0FGL J1615.6–5049 is spatially coincident with HESS J1616–508, which has been suspected being the PWN of PSR J1617–5055 (Landi et al. 2007), (Kargaltsev et al. 2009).
- 0FGL J1741.4–3046 is spatially consistent with the unidentified HESS J1741–302. (Tibolla et al. 2008). See the note in the previous section about LAT analysis in the Galactic Center region.
- 0FGL J1805.3–2138 is spatially coincident with HESS J1804–216 (Aharonian et al. 2005). Formally still unidentified, HESS J1804–216 has been noted for possible counterparts in SNR G8.7–0.1, W30, or PSR J1803–2137. At this stage, we are not able to make a firm identification of the LAT source with any of the counterpart hypotheses.
- 0FGL J1814.3–1739 is spatially coincident with HESS J1813–178 (Aharonian et al. 2005), which has been classified as a composite SNR, characterized by a shell-type SNR with central PWN candidate, not to be distinguishable given the angular resolution of present VHE observatories. At this stage, we are not able to settle either on a SNR or on a PSR/PWN scenario for connecting HESS J1813–178 with the LAT source, leaving this study to a follow-up investigation.
- 0FGL J1834.4–0841 is spatially coincident with HESS J1834–087 (Aharonian et al. 2005). Formally still unidentified, HESS J1834–087 was proposed to be explained in emission scenarios involving SNR W41, hadronic interactions with a giant molecular cloud, and/or PSR J1833–0827. See Table 2. PSR J1833–0827 is not consistent in position with the LAT source. At this stage, we are not able to draw conclusions on a possible connection of the LAT source to the presented counterpart hypothesis.
- 0FGL J1923.0+1411 is spatially coincident with HESS J1923+141, which is also spatially consistent with SNR G49.2–0.7 (W51). See Sec. 4.2.3 and Table 2 for a discussion of LAT source associations with SNRs and PWNe.

- 0FGL J2032.2+4122, conclusively identified as a PSR, is spatially coincident with TeV 2032+4130 seen by HEGRA (Aharonian et al. 2002) and Milagro source MGRO J2031+41 (Abdo et al. 2007). Formally still unidentified, TeV J2032+4130 was noted for being close to the direction of the massive stellar cluster association Cygnus OB2. MGRO J2031+41, also unidentified, was reported as an extended and possibly confused source that could only be explained in part by the emission from TeV 2032+4130. We leave the possible association of LAT PSR J2032+41 with TeV J2032+4130 or MGRO 2031+41 to a detailed subsequent study.
- Finally, it is noteworthy that LAT pulsars are found also in the error circles of four Milagro detected or candidate sources (Abdo et al. 2007):
 - 0FGL J2020.8+3649 (MGRO 2019+37)
 - 0FGL J1907.5+6002 (MGRO 1908+06)
 - 0FGL J0634.0+1745 (C3 - candidate, Geminga)
 - 0FGL J2229.0+6114 (C4 - candidate)

Detailed discussion of individual sources is beyond the scope of this paper. By noting these positional coincidences, we call attention to areas of work still in progress on the *Fermi* LAT data. The 0FGL list is a starting point for additional research in many areas.

The *Fermi* LAT Collaboration acknowledges generous ongoing support from a number of agencies and institutes that have supported both the development and the operation of the LAT as well as scientific data analysis. These include the National Aeronautics and Space Administration and the Department of Energy in the United States, the Commissariat à l’Energie Atomique and the Centre National de la Recherche Scientifique / Institut National de Physique Nucléaire et de Physique des Particules in France, the Agenzia Spaziale Italiana and the Istituto Nazionale di Fisica Nucleare in Italy, the Ministry of Education, Culture, Sports, Science and Technology (MEXT), High Energy Accelerator Research Organization (KEK) and Japan Aerospace Exploration Agency (JAXA) in Japan, and the K. A. Wallenberg Foundation, the Swedish Research Council and the Swedish National Space Board in Sweden.

Additional support for science analysis during the operations phase from the following agencies is also gratefully acknowledged: the Istituto Nazionale di Astrofisica in Italy and the K. A. Wallenberg Foundation in Sweden for providing a grant in support of a Royal Swedish Academy of Sciences Research fellowship for JC.

This work made extensive use of the ATNF pulsar catalogue (Manchester et al. 2005)⁸.

The LAT team extends thanks to the anonymous referee who made many valuable suggestions of ways to improve this paper.

Facilities: Fermi LAT.

REFERENCES

- Abdo, A. A., et al. 2009a, *Science*, 323, 1688
- . 2009b, *ApJ*, 696, 1084
- . 2008, *Science*, 322, 1218
- . 2009c, *ApJ*, in press - “Bright AGN Source List from the First Three Months of the Fermi Large Area Telescope All-Sky Survey,” arXiv:0902.1559
- . 2009d, *Science*, submitted - “Discovery of a Population of Gamma-ray Millisecond Pulsars with the Fermi Large Area Telescope”
- . 2009e, *ApJ*, in preparation - “Discovery of high-energy gamma-ray emission from the globular cluster 47 Tucanae with Fermi”
- . 2009f, *ApJ*, 695, L72
- . 2009g, *ApJ*, in press - “Early Fermi Gamma-ray Space Telescope Observations of the Quasar 3C 454.3,” arXiv:0904.4280
- . 2009h, *ApJ*, in press - “Fermi Discovery of Gamma-Ray Emission from NGC1275,” arXiv:0904.1904
- . 2009i, *ApJ*, in preparation - “Fermi LAT detection of pulsed gamma-rays from the Vela-like pulsars PSR J1048–5832 and PSR J2229+6114”
- . 2009j, *ApJ*, submitted - “Fermi LAT Observations of LS I +61° 303: First Detection of an Orbital Modulation in GeV Gamma Rays”
- . 2009k, *ApJ*, in press - “Fermi/LAT discovery of gamma-ray emission from a relativistic jet in the Narrow-Line Quasar PMN J0948+0022”

⁸<http://www.atnf.csiro.au/research/pulsar/psrcat>

- . 2009l, ApJ, in press - “Fermi/LAT discovery of gamma-ray emission from the flat-spectrum radio quasar PKS 1454–354,” arXiv0903.1713
- . 2009m, ApJ, in preparation - “PKS 1502+106: a new and distant gamma-ray blazar in outburst discovered by the Fermi Large Area Telescope”
- . 2009n, ApJ, submitted - “Pulsed gamma-rays from PSR J2021+3651 with the Fermi Large Area Telescope”
- . 2009o, ApJ, in press - “Pulsed Gamma-rays from the millisecond pulsar J0030+0451 with the Fermi Large Area Telescope,” arXiv:0904.4377
- . 2009p, Science, submitted - “Sixteen Gamma-Ray Pulsars Discovered in Blind Frequency Searches Using the Fermi LAT”
- . 2009q, ApJ, submitted - “The On-orbit calibration of the Fermi Large Area Telescope”, arXiv:0904.2226v1
- . 2007, ApJ, 664, L91, - ”TeV Gamma-Ray Sources from a Survey of the Galactic Plane with Milagro”

Aharonian, F., et al. 2002, A&A, 393, L37

—. 2009, ApJ, 696, L150

—. 2005, Science, 307, 1938

—. 2007, A&A, 467, 1075

—. 2006a, A&A, 456, 245

—. 2006b, A&A, 460, 743

Albert, J., et al. 2008, ApJ, 684, 1351

Atwood, W. B., et al. 2009, ApJ, in press

Bertin, E., & Arnouts, S. 1996, A&AS, 117, 393

Calabretta, M. R., & Greisen, E. W. 2002, A&A, 395, 1077

Casandjian, J.-M., & Grenier, I. A. 2008, A&A, 489, 849

Cheung, C. C., Reyes, L., Longo, F., & Iafate, G. 2008, The Astronomer’s Telegram, 1788,

- Ciprini, S., et al. 2007, in American Institute of Physics Conference Series, Vol. 921, The First GLAST Symposium, ed. S. Ritz, P. Michelson, & C. A. Meegan, 546–547
- Damiani, F., Maggio, A., Micela, G., & Sciortino, S. 1997, *ApJ*, 483, 350
- de Ruiter, H. R., Arp, H. C., & Willis, A. G. 1977, *A&AS*, 28, 211
- Funk, S. 2005, in International Cosmic Ray Conference, Vol. 4, International Cosmic Ray Conference, 123–+
- Green, D. A. 2006, Astrophysics Group - Cavendish Laboratory, Cambridge, UK, sNR Catalog
- Guibert, J., Lequeux, J., & Viallefond, F. 1978, *A&A*, 68, 1
- Harris, W. E. 1997, VizieR Online Data Catalog, 7202, 0
- Hartman, R. C., et al. 1999, *ApJS*, 123, 79
- Healey, S. E., et al. 2008, *ApJS*, 175, 97
- Healey, S. E., Romani, R. W., Taylor, G. B., Sadler, E. M., Ricci, R., Murphy, T., Ulvestad, J. S., & Winn, J. N. 2007, *ApJS*, 171, 61
- Hermesen, W., et al. 1977, *Nature*, 269, 494
- Hunter, S. D., et al. 1997, *ApJ*, 481, 205
- Kargaltsev, O., Pavlov, G. G., & Wong, J. A. 2009, *ApJ*, 690, 891
- Landi, R., de Rosa, A., Dean, A. J., Bassani, L., Ubertini, P., & Bird, A. J. 2007, *MNRAS*, 380, 926
- Liu, Q. Z., van Paradijs, J., & van den Heuvel, E. P. J. 2006, *A&A*, 455, 1165
- . 2007, VizieR Online Data Catalog, 346, 90807
- Manchester, R. N., Hobbs, G. B., Teoh, A., & Hobbs, M. 2005, *AJ*, 129, 1993
- Massaro, E., Giommi, P., Leto, C., Marchegiani, P., Maselli, A., Perri, M., Piranomonte, S., & Sclavi, S. 2009, *A&A*, in press, 2009 - BZ Catalog, arXiv0810.2206
- Mattox, J. R., et al. 1996, *ApJ*, 461, 396
- Paredes, J. M. 2006, ArXiv Astrophysics e-prints

- Pittori, C., et al. 2009, A&A, in press - AGILE Catalog
- Porter, T. A., Moskalenko, I. V., Strong, A. W., Orlando, E., & Bouchet, L. 2008, ApJ, 682, 400
- Protassov, R., van Dyk, D. A., Connors, A., Kashyap, V. L., & Siemiginowska, A. 2002, ApJ, 571, 545
- Roberts, M. S. E. 2005, McGill University, Montreal, Quebec, Canada, pWN Catalog
- Smith, D. A., et al. 2008, A&A, 492, 923
- Sowards-Emmerd, D., Romani, R. W., & Michelson, P. F. 2003, ApJ, 590, 109
- Starck, J.-L., & Pierre, M. 1998, A&AS, 128, 397
- Strong, A. W. 2007, Ap&SS, 309, 35
- Strong, A. W., Moskalenko, I. V., & Reimer, O. 2004, ApJ, 613, 962
- Sutherland, W., & Saunders, W. 1992, MNRAS, 259, 413
- Swanenburg, B. N., et al. 1981, ApJ, 243, L69
- Thompson, D. J., et al. 1993, ApJS, 86, 629
- Thompson, D. J., Simpson, G. A., & Özel, M. E. 1981, J. Geophys. Res., 86, 1265
- Tibolla, O., Komin, N., Kosack, K., & Naumann-Godo, M. 2008, in American Institute of Physics Conference Series, Vol. 1085, American Institute of Physics Conference Series, ed. F. A. Aharonian, W. Hofmann, & F. Rieger, 249–252
- Torres, D. F., Romero, G. E., Dame, T. M., Combi, J. A., & Butt, Y. M. 2003, Phys. Rep., 382, 303
- Tramacere, A., & Rea, N. 2009, The Astronomer’s Telegram, 1888, 1

Table 6. LAT Bright Source List

Name 0FGL	R.A.	Decl.	l	b	θ_{95}	100 MeV – 1 GeV			1 GeV – 100 GeV			Var.	γ -ray Assoc.	Class	ID or Assoc.	Ref.	
						\sqrt{TS}	F_{23}	ΔF_{23}	$\sqrt{TS_{23}}$	F_{35}	ΔF_{35}						$\sqrt{TS_{35}}$
J0007.4+7303	1.852	73.065	119.690	10.471	0.054	64.6	32.4	1.3	36.2	6.14	0.27	55.9	...	3EG J0010+7309 EGR J0008+7308 1AGL J0006+7311	PSR	LAT PSR J0007+7303	1
J0017.4–0503	4.358	–5.054	101.273	–66.485	0.252	14.7	11.8	1.4	15.3	0.27	0.07	7.1	T	...	bzq	CGRaBS J0017–0512	...
J0025.1–7202	6.295	–72.042	305.786	–44.940	0.163	12.7	5.1	2.0	6.8	0.56	0.10	11.5	glb	NGC 104 47 Tuc	2
J0030.3+0450	7.600	4.848	113.111	–57.622	0.138	18.7	8.9	0.0	13.6	0.71	0.10	14.9	PSR	PSR J0030+0451	3, 4
J0033.6–1921	8.401	–19.360	94.215	–81.220	0.147	10.7	1.4	0.0	4.6	0.36	0.07	10.1	bzb	BZB J0033–1921 KUV 00311–1938	...
J0036.7+5951	9.177	59.854	121.081	–2.965	0.144	10.3	6.7	3.1	5.6	0.48	0.10	8.6	bzb	BZB J0035+5950 IES 0033+595	...
J0050.5–0928	12.637	–9.470	122.209	–72.341	0.130	20.5	8.1	1.3	15.6	0.72	0.10	14.9	T	...	bzb	CGRaBS J0050–0929 PKS 0048–097	...
J0051.1–0647	12.796	–6.794	122.751	–69.666	0.127	15.7	6.6	1.4	10.4	0.57	0.09	12.0	T	...	bzq	CGRaBS J0051–0650 PKS 0048–071	...
J0100.2+0750	15.051	7.844	126.716	–54.963	0.110	11.1	2.5	0.0	2.8	0.31	0.07	10.4	bzu	CRATES J0100+0745	...
J0112.1+2247	18.034	22.789	129.148	–39.832	0.134	17.6	5.4	0.7	10.8	0.65	0.09	14.4	bzb	CGRaBS J0112+2244 S2 0109+22	...
J0118.7–2139	19.676	–21.656	172.990	–81.728	0.164	17.8	7.0	1.1	14.5	0.52	0.09	12.2	T	...	bzq	CGRaBS J0118–2141 PKS 0116–219	...
J0120.5–2703	20.128	–27.056	213.951	–83.529	0.140	11.8	2.3	0.8	6.6	0.33	0.07	10.3	bzb	CGRaBS J0120–2701 PKS 0118–272	...
J0136.6+3903	24.163	39.066	132.446	–22.969	0.087	12.5	5.9	0.0	3.6	0.45	0.08	12.3	bzb	BZB J0136+3905 B3 0133+388	...
J0137.1+4751	24.285	47.854	130.818	–14.317	0.120	18.8	10.0	1.6	12.3	0.78	0.10	15.4	T	...	bzq	CGRaBS J0136+4751 DA 55	...
J0144.5+2709	26.142	27.159	137.248	–34.231	0.209	10.4	1.7	0.5	6.6	0.32	0.07	7.4	bzb	CRATES J0144+2705 TXS 0141+268	...
J0145.1–2728	26.289	–27.478	217.694	–78.067	0.243	13.4	9.2	1.3	13.7	0.26	0.07	6.9	T	...	bzq	CGRaBS J0145–2733 PKS 0142–278	...
J0204.8–1704	31.219	–17.068	186.072	–70.274	0.163	16.6	10.2	1.3	15.0	0.44	0.08	10.8	bzq	CGRaBS J0204–1701 PKS 0202–17	...

Table 6—Continued

Name 0FGL	R.A.	Decl.	l	b	θ_{95}	\sqrt{TS}	100 MeV – 1 GeV			1 GeV – 100 GeV			Var.	γ -ray Assoc.	Class	ID or Assoc.	Ref.
							F_{23}	ΔF_{23}	$\sqrt{TS_{23}}$	F_{35}	ΔF_{35}	$\sqrt{TS_{35}}$					
J0210.8–5100	32.706	–51.013	276.083	–61.776	0.070	34.1	21.4	1.2	28.2	1.35	0.14	22.2	T	3EG J0210–5055 EGR J0210–5058	bzq	CGRaBS J0210–5101 PKS 0208–512	...
J0217.8+0146	34.467	1.768	162.139	–54.389	0.106	21.7	8.9	1.2	16.1	0.82	0.11	16.7	T	...	bzq	CGRaBS J0217+0144 PKS 0215+015	...
J0220.9+3607	35.243	36.121	142.504	–23.325	0.225	12.3	10.7	1.3	13.1	0.22	0.06	6.0	bzq	CGRaBS J0221+3556 B2 0218+35	...
J0222.6+4302	35.653	43.043	140.132	–16.763	0.054	47.4	24.0	1.4	32.0	2.61	0.18	37.4	T	3EG J0222+4253 EGR J0223+4300	bzb	BZB J0222+4302 3C 66A	...
J0229.5–3640	37.375	–36.681	243.801	–67.189	0.138	19.2	13.7	1.5	16.9	0.45	0.08	10.9	T	...	bzq	BZQ J0229–3643 PKS 0227–369	...
J0238.4+2855	39.600	28.923	149.521	–28.368	0.193	10.9	8.3	1.6	9.3	0.34	0.08	7.5	bzq	CGRaBS J0237+2848 B2 0234+28	...
J0238.6+1636	39.663	16.613	156.775	–39.112	0.052	85.7	60.7	2.1	64.3	6.81	0.29	62.5	T	3EG J0237+1635	bzb	CGRaBS J0238+1636 AO 0235+164	...
J0240.3+6113	40.093	61.225	135.661	1.075	0.069	42.3	70.3	2.5	37.4	3.34	0.23	27.6	T	EGR J0240+6112 1AGL J0242+6111	HXB	LS I+61 303	47 5
J0245.6–4656	41.423	–46.934	262.019	–60.098	0.192	11.4	5.3	0.8	9.0	0.32	0.07	8.1	bzu	CRATES J0246–4651 PKS 0244–470	...
J0303.7–2410	45.940	–24.176	214.764	–60.119	0.174	12.3	2.5	0.9	7.8	0.38	0.08	10.2	bzb	CRATES J0303–2407 PKS 0301–243	...
J0320.0+4131	50.000	41.524	150.601	–13.230	0.086	29.7	16.6	1.4	21.6	1.60	0.15	22.6	T	...	rdg	CGRaBS J0319+4130 NGC 1275	6
J0334.1–4006	53.546	–40.107	244.710	–54.088	0.152	13.2	4.5	1.4	9.0	0.39	0.08	10.7	bzb	CGRaBS J0334–4008 PKS 0332–403	...
J0349.8–2102	57.465	–21.046	214.385	–49.035	0.157	21.2	16.7	1.6	20.4	0.56	0.09	10.9	bzq	CGRaBS J0349–2102 PKS 0347–211	...
J0357.5+3205	59.388	32.084	162.712	–16.056	0.147	14.9	10.4	1.8	13.6	0.64	0.10	10.5	PSR	LAT PSR J0357+32	7
J0407.6–3829	61.923	–38.491	241.360	–47.751	0.142	13.5	6.5	1.3	11.2	0.41	0.08	9.6	T	...	bzq	CRATES J0406–3826 PKS 0405–385	...
J0412.9–5341	63.230	–53.686	263.001	–44.716	0.206	10.7	5.7	1.3	8.8	0.29	0.07	7.9	bzu	CRATES J0413–5332	...
J0423.1–0112	65.785	–1.204	195.131	–33.092	0.143	11.5	10.1	3.1	10.3	0.38	0.08	8.8	...	3EG J0422–0102	bzq	CGRaBS J0423–0120 PKS 0420–014	...
J0428.7–3755	67.193	–37.923	240.689	–43.597	0.079	39.6	21.1	1.6	28.4	1.99	0.17	29.6	bzb	CGRaBS J0428–3756	...

Table 6—Continued

Name 0FGL	R.A.	Decl.	l	b	θ_{95}	\sqrt{TS}	100 MeV – 1 GeV			1 GeV – 100 GeV			Var.	γ -ray Assoc.	Class	ID or Assoc.	Ref.
							F_{23}	ΔF_{23}	$\sqrt{TS_{23}}$	F_{35}	ΔF_{35}	$\sqrt{TS_{35}}$					
J0449.7–4348	72.435	–43.815	248.780	–39.859	0.082	28.4	10.9	1.4	16.9	1.25	0.13	23.8	bzb	PKS 0426–380 CRATES J0449–4350	...
J0457.1–2325	74.288	–23.432	223.739	–34.880	0.065	52.3	34.0	1.8	43.0	2.61	0.19	34.5	T	3EG J0456–2338 EGR J0456–2334	bzq	PKS 0447–439 CGRaBS J0457–2324	...
J0507.9+6739	76.985	67.650	143.772	15.905	0.058	13.2	5.4	0.0	4.8	0.27	0.06	12.5	bzb	PKS 0454–234 BZB J0507+6737	...
J0516.2–6200	79.063	–62.000	271.376	–34.834	0.181	11.2	10.4	0.0	6.7	0.42	0.08	10.0	...	3EG J0512–6150	bzu	1ES 0502+675 CGRaBS J0516–6207	...
J0531.0+1331	82.761	13.528	191.385	–10.992	0.133	17.3	22.9	2.1	16.5	0.76	0.12	10.6	T	3EG J0530+1323 EGR J0530+1331	bzq	PKS 0516–621 CGRaBS J0530+1331	...
J0534.6+2201	83.653	22.022	184.562	–5.764	0.046	139.2	204.0	9.2	116.6	15.40	0.44	92.9	...	3EG J0534+2200 EGR J0534+2159 1AGL J0535+2205	PSR pwn	PKS 0528+134 PSR J0534+2200 Crab	...
J0538.4–6856	84.612	–68.940	279.281	–31.713	0.325	17.8	19.1	2.6	18.4	0.64	0.12	9.5	...	3EG J0533–6916	...	LMC	...
J0538.8–4403	84.725	–44.062	250.057	–31.075	0.072	48.6	31.7	1.8	38.8	2.51	0.19	32.5	T	3EG J0540–4402 EGR J0540–4358 1AGL J0538–4424	bzb	CRATES J0538–4405 PKS 0537–441	...
J0613.9–0202	93.485	–2.047	210.468	–9.274	0.175	10.0	6.8	2.3	6.2	0.47	0.09	8.5	PSR	PSR J0613–0200	4
J0614.3–3330	93.577	–33.500	240.513	–21.801	0.083	28.9	5.4	0.2	15.7	1.64	0.15	25.4	...	3EG J0616–3310 EGR J0615–3308
J0617.4+2234	94.356	22.568	189.079	3.066	0.063	50.7	43.1	2.5	36.2	4.99	0.27	38.8	...	3EG J0617+2238 EGR J0617+2238 1AGL J0617+2236	†
J0631.8+1034	97.955	10.570	201.302	0.507	0.151	10.4	6.9	3.0	6.4	0.74	0.13	8.8	PSR	PSR J0631+1036	...
J0633.5+0634	98.387	6.578	205.041	–0.957	0.105	23.4	18.9	2.5	17.4	1.60	0.17	16.9	...	EGR J0633+0646	PSR	LAT PSR J0633+0632	7
J0634.0+1745	98.503	17.760	195.155	4.285	0.043	283.2	286.2	3.8	206.0	61.61	0.86	207.7	...	3EG J0633+1751 EGR J0633+1750 1AGL J0634+1748	PSR	PSR J0633+1746 Geminga	...
J0643.2+0858	100.823	8.983	204.010	2.290	0.121	15.7	22.2	2.8	15.8	0.84	0.14	9.9	T
J0654.3+4513	103.590	45.220	171.228	19.369	0.075	29.2	19.1	1.6	22.5	1.26	0.13	20.4	T	...	bzq	CGRaBS J0654+4514 B3 0650+453	...
J0654.3+5042	103.592	50.711	165.676	21.107	0.083	15.6	4.3	1.2	8.0	0.59	0.09	13.9	T	...	bzu	CGRaBS J0654+5042	...

Table 6—Continued

Name 0FGL	R.A.	Decl.	l	b	θ_{95}	\sqrt{TS}	100 MeV – 1 GeV			1 GeV – 100 GeV			Var.	γ -ray Assoc.	Class	ID or Assoc.	Ref.
							F_{23}	ΔF_{23}	$\sqrt{TS_{23}}$	F_{35}	ΔF_{35}	$\sqrt{TS_{35}}$					
J0700.0–6611	105.016	–66.199	276.778	–23.809	0.182	10.1	3.5	0.0	5.6	0.44	0.09	8.6	bzu	CRATES J0700–6610 PKS 0700–661	...
J0712.9+5034	108.231	50.575	166.688	23.900	0.146	11.2	3.0	0.7	6.1	0.36	0.08	9.6	T	...	bzb	CGRaBS J0712+5033	...
J0714.2+1934	108.552	19.574	197.685	13.648	0.128	15.0	9.5	1.6	12.0	0.51	0.09	10.6	T	...	bzq	CLASS J0713+1935	...
J0719.4+3302	109.869	33.037	185.139	19.855	0.141	12.3	7.1	1.5	9.8	0.37	0.08	8.9	T	...	bzq	CRATES J0719+3307 TXS 0716+332	...
J0722.0+7120	110.508	71.348	143.976	28.029	0.080	34.4	15.5	1.6	22.9	1.49	0.13	27.6	T	3EG J0721+7120 EGR J0723+7134 1AGL J0722+7125	bzb	CGRaBS J0721+7120 S5 0716+71	...
J0730.4–1142	112.607	–11.707	227.799	3.154	0.082	28.9	26.2	2.2	21.6	1.74	0.16	21.7	T	...	bzq	BZQ J0730–1141 PKS 0727–11	...
J0738.2+1738	114.575	17.634	201.933	18.081	0.137	11.9	3.3	1.4	8.2	0.34	0.08	9.3	...	3EG J0737+1721 EGR J0737+1720	bzb	CGRaBS J0738+1742 PKS 0735+178	...
J0818.3+4222	124.579	42.367	178.244	33.409	0.083	20.9	6.2	1.1	12.4	0.79	0.11	16.7	bzb	CGRaBS J0818+4222 OJ 425	...
J0824.9+5551	126.239	55.859	161.981	35.142	0.214	10.6	10.7	1.3	11.5	0.17	0.05	5.2	T	...	bzq	CGRaBS J0824+5552 TXS 0820+560	...
J0826.0–2228	126.500	–22.480	243.964	8.941	0.144	12.7	5.1	1.3	8.2	0.50	0.09	10.6	bzb	BZB J0826–2230 PKS 0823–223	...
J0835.4–4510	128.865	–45.170	263.560	–2.767	0.042	374.2	803.1	5.7	295.9	112.08	1.23	255.6	...	3EG J0834–4511 EGR J0834–4512 1AGL J0835–4509	PSR	PSR J0835–4510 Vela	8
J0855.4+2009	133.857	20.162	206.810	35.974	0.178	15.1	7.4	1.3	12.3	0.43	0.08	10.0	...	3EG J0853+1941	bzb	CGRaBS J0854+2006 OJ 287	...
J0909.7+0145	137.446	1.757	228.640	31.262	0.273	11.6	9.3	0.3	12.5	0.19	0.06	5.1	bzb	CGRaBS J0909+0200 PKS 0907+022	...
J0910.2–5044	137.568	–50.743	271.569	–1.856	0.161	13.2	29.4	3.3	12.3	1.10	0.18	8.7	T
J0921.2+4437	140.320	44.617	175.809	44.876	0.128	15.2	8.8	1.4	12.5	0.42	0.08	10.8	bzq	CGRaBS J0920+4441 RGB J0920+446	...
J0948.3+0019	147.077	0.317	236.530	38.549	0.287	12.8	8.9	1.4	12.6	0.24	0.07	5.9	T	...	bzq	CGRaBS J0948+0022 PMN J0948+0022	9
J0957.6+5522	149.424	55.375	158.605	47.939	0.092	24.0	8.4	1.3	17.0	0.79	0.10	18.8	...	EGR J0957+5513	bzq	CRATES J0957+5522 4C +55.17	...

Table 6—Continued

Name 0FGL	R.A.	Decl.	l	b	θ_{95}	\sqrt{TS}	100 MeV – 1 GeV			1 GeV – 100 GeV			Var.	γ -ray Assoc.	Class	ID or Assoc.	Ref.
							F_{23}	ΔF_{23}	$\sqrt{TS_{23}}$	F_{35}	ΔF_{35}	$\sqrt{TS_{35}}$					
J1012.9+2435	153.241	24.598	207.897	54.406	0.175	12.4	4.2	0.9	9.2	0.35	0.08	8.6	T	...	bzq	CRATES J1012+2439	...
J1015.2+4927	153.809	49.463	165.473	52.727	0.062	23.8	7.9	1.5	10.7	1.00	0.11	22.4	bzb	CGRaBS J1015+4926	...
J1015.9+0515	153.991	5.254	236.457	47.036	0.104	20.6	12.4	1.5	17.7	0.67	0.10	14.3	T	...	bzq	1ES 1011+496 CRATES J1016+0513 PMN J1016+0512	...
J1018.2–5858	154.564	–58.978	284.298	–1.765	0.113	22.4	36.7	4.8	16.9	3.06	0.27	17.7	...	3EG J1013–5915	†
J1024.0–5754	156.001	–57.903	284.346	–0.453	0.106	13.9	42.0	0.0	10.8	2.55	0.29	13.2
J1028.6–5817	157.166	–58.292	285.074	–0.459	0.079	16.0	27.6	0.0	9.1	2.56	0.28	15.3	...	3EG J1027–5817	PSR	PSR J1028–5819	10
J1034.0+6051	158.504	60.853	147.765	49.122	0.209	14.8	7.1	1.3	12.8	0.33	0.07	9.4	bzq	CGRaBS J1033+6051	...
J1045.6–5937	161.409	–59.631	287.637	–0.548	0.123	19.5	30.7	4.6	15.5	2.29	0.25	14.8	...	1AGL J1043–5931
J1047.6–5834	161.922	–58.577	287.385	0.508	0.138	18.5	43.9	0.0	13.4	2.53	0.25	16.8	...	3EG J1048–5840 EGR J1048–5839	PSR	PSR J1048–5832	11
J1053.7+4926	163.442	49.449	160.309	58.263	0.124	10.1	4.0	0.0	0.8	0.21	0.05	10.2	bzb	BZB J1053+4929 MS 1050.7+4946	50 ...
J1054.5+2212	163.626	22.215	216.968	63.049	0.178	11.2	4.0	1.0	7.8	0.29	0.07	8.9	bzb	CLASS J1054+2210	...
J1057.8+0138	164.451	1.643	251.219	52.709	0.194	10.3	8.8	1.7	8.4	0.35	0.08	8.3	bzq	CGRaBS J1058+0133	...
J1058.1–5225	164.527	–52.432	285.995	6.673	0.073	43.7	25.6	2.0	31.2	4.07	0.25	33.8	...	3EG J1058–5234 EGR J1058–5221 1AGL J1058–5239	PSR	PKS 1055+018 PSR J1057–5226	...
J1058.9+5629	164.731	56.488	149.521	54.442	0.083	12.0	4.7	1.8	8.2	0.33	0.07	10.0	bzb	CGRaBS J1058+5628 RXS J10586+5628	...
J1100.2–8000	165.057	–80.012	298.047	–18.212	0.285	12.1	10.8	2.2	10.3	0.31	0.08	6.3	T	...	bzb	CGRaBS J1058–8003 PKS 1057–79	...
J1104.5+3811	166.137	38.187	179.868	65.056	0.055	47.1	13.3	1.3	23.9	2.61	0.17	40.9	...	3EG J1104+3809 EGR J1104+3813 1AGL J1104+3754	bzb	CGRaBS J1104+3812 Mrk 421	...
J1106.4–6055	166.605	–60.918	290.516	–0.604	0.251	10.8	16.9	5.2	8.6	1.43	0.22	9.0	...	3EG J1102–6103 1AGL J1108–6103	†
J1115.8–6108	168.967	–61.147	291.661	–0.384	0.214	12.1	25.7	5.3	11.1	1.53	0.23	9.4
J1123.0–6416	170.762	–64.268	293.519	–3.024	0.125	10.2	22.4	3.9	8.8	0.39	0.13	5.1	T
J1129.8–1443	172.454	–14.727	275.133	43.694	0.246	10.5	10.6	1.6	11.7	0.20	0.06	5.7	bzq	CRATES J1130–1449	...

Table 6—Continued

Name 0FGL	R.A.	Decl.	l	b	θ_{95}	\sqrt{TS}	100 MeV – 1 GeV			1 GeV – 100 GeV			Var.	γ -ray Assoc.	Class	ID or Assoc.	Ref.
							F_{23}	ΔF_{23}	$\sqrt{TS_{23}}$	F_{35}	ΔF_{35}	$\sqrt{TS_{35}}$					
J1146.7–3808	176.689	–38.149	289.170	22.988	0.185	10.4	3.1	1.2	6.5	0.38	0.08	8.2	bzq	PKS 1127–14 CGRaBS J1147–3812 PKS 1144–379	...
J1159.2+2912	179.800	29.216	199.605	78.307	0.192	14.6	9.1	1.0	13.9	0.29	0.07	7.7	...	3EG J1200+2847	bzq	CGRaBS J1159+2914 4C 29.45	...
J1218.0+3006	184.517	30.108	188.826	82.097	0.099	27.4	9.0	1.0	14.9	1.41	0.14	24.1	T	...	bzb	CGRaBS J1217+3007 B2 1215+30	...
J1221.7+2814	185.439	28.243	201.593	83.336	0.101	24.0	6.5	0.8	13.1	1.03	0.12	20.6	T	1AGL J1222+2851	bzb	CGRaBS J1221+2813 W Com	...
J1229.1+0202	187.287	2.045	289.975	64.355	0.083	52.0	63.9	2.6	54.2	1.61	0.14	25.7	T	3EG J1229+0210 EGR J1229+0203 1AGL J1228+0142	bzq	CGRaBS J1229+0203 3C 273	...
J1231.5–1410	187.875	–14.179	295.642	48.410	0.087	30.9	9.3	1.2	18.8	1.71	0.15	25.6	...	EGR J1231–1412
J1246.6–2544	191.655	–25.734	301.571	37.125	0.168	11.7	7.2	1.4	9.1	0.37	0.08	8.8	bzq	CGRaBS J1246–2547 PKS 1244–255	...
J1248.7+5811	192.189	58.191	123.617	58.934	0.122	14.3	7.0	1.6	9.9	0.39	0.07	12.2	bzb	PG 1246+586	...
J1253.4+5300	193.369	53.001	122.229	64.125	0.154	12.1	5.2	1.5	8.1	0.33	0.07	9.6	bzb	CRATES J1253+5301 S4 1250+53	...
J1256.1–0547	194.034	–5.800	305.081	57.052	0.079	36.8	28.3	1.8	31.8	1.44	0.14	22.6	T	3EG J1255–0549 EGR J1256–0552 1AGL J1256–0549	bzq	CGRaBS J1256–0547 3C 279	...
J1310.6+3220	197.656	32.339	85.458	83.331	0.103	27.3	15.5	1.1	22.8	0.93	0.11	19.2	T	...	bzq	CGRaBS J1310+3220 B2 1308+32	...
J1311.9–3419	197.998	–34.318	307.754	28.361	0.204	12.5	14.5	0.0	9.9	0.66	0.11	10.9	...	3EG J1314–3431 EGR J1314–3417
J1325.4–4303	201.353	–43.062	309.501	19.376	0.304	12.4	21.9	2.4	14.9	0.32	0.09	5.7	...	3EG J1324–4314	rdg	BZU J1325–4301 NGC 5128, Cen A	...
J1326.6–5302	201.651	–53.047	308.277	9.460	0.191	13.2	16.9	0.0	10.3	0.69	0.12	9.5
J1328.8–5604	202.222	–56.079	308.174	6.411	0.142	10.6	16.0	4.3	8.6	0.66	0.13	8.8	T
J1331.7–0506	202.935	–5.112	321.247	56.320	0.278	14.3	10.4	1.2	14.6	0.34	0.08	7.4	T	...	bzq	CGRaBS J1332–0509 PKS 1329–049	...
J1333.3+5058	203.331	50.973	107.300	64.865	0.219	12.4	8.8	1.3	11.5	0.28	0.07	7.9	bzq	CLASS J1333+5057	...
J1355.0–1044	208.764	–10.735	327.221	49.113	0.163	11.5	8.4	1.3	9.7	0.30	0.07	8.0	T	...	bzq	CRATES J1354–1041	...

Table 6—Continued

Name 0FGL	R.A.	Decl.	l	b	θ_{95}	100 MeV – 1 GeV			1 GeV – 100 GeV			Var.	γ -ray Assoc.	Class	ID or Assoc.	Ref.	
						\sqrt{TS}	F_{23}	ΔF_{23}	$\sqrt{TS_{23}}$	F_{35}	ΔF_{35}						$\sqrt{TS_{35}}$
J1413.1–6203	213.292	–62.063	312.346	–0.695	0.096	16.8	47.1	21.5	12.8	2.59	0.30	13.0	...	EGRc J1414–6224 1AGL J1412–6149	...	PKS 1352–104	...
J1418.8–6058	214.718	–60.979	313.338	0.113	0.074	25.8	46.0	22.9	18.3	5.42	0.38	22.1	...	1AGL J1419–6055	PSR	LAT PSR J1418–6058	7
J1427.1+2347	216.794	23.785	29.472	68.166	0.073	24.1	4.2	1.0	10.1	0.92	0.11	21.4	bzb	CRATES J1427+2347	...
J1430.5–5918	217.634	–59.301	315.288	1.173	0.119	10.4	29.7	12.1	9.9	1.26	0.21	8.7
J1457.6–3538	224.407	–35.639	329.936	20.530	0.076	39.6	30.1	0.5	32.7	2.00	0.17	26.0	T	3EG J1500–3509	bzq	CGRaBS J1457–3539	12
J1459.4–6056	224.874	–60.937	317.863	–1.833	0.119	15.9	25.0	11.8	12.0	1.26	0.19	10.1	PSR	LAT PSR J1459–60	6
J1504.4+1030	226.115	10.505	11.409	54.577	0.054	88.2	63.4	2.1	71.8	5.86	0.26	58.9	T	...	bzq	CGRaBS J1504+1029	13
J1509.5–5848	227.390	–58.812	320.003	–0.596	0.121	12.8	45.9	0.0	7.9	2.11	0.26	11.4	...	1AGL J1506–5859	PSR	PSR J1509–5850	...
J1511.2–0536	227.814	–5.613	354.099	42.948	0.252	10.8	8.3	1.7	8.9	0.34	0.08	7.1	bzq	PKS 1508–05 BZQ J1510–0543	...
J1512.7–0905	228.196	–9.093	351.282	40.153	0.087	45.0	48.8	2.3	44.0	1.84	0.16	23.8	T	3EG J1512–0849 EGR J1512–0857 1AGL J1511–0908	bzq	PKS 1510–08 BZQ J1512–0905	...
J1514.3–4946	228.585	–49.769	325.254	6.807	0.120	11.0	14.9	0.0	7.2	0.71	0.12	9.8
J1517.9–2423	229.496	–24.395	340.724	27.521	0.101	12.3	4.8	0.6	7.5	0.39	0.08	10.5	bzb	CGRaBS J1517–2422	...
J1522.2+3143	230.552	31.726	50.143	57.014	0.087	34.3	21.2	1.5	30.3	1.06	0.11	20.7	T	...	bzq	CGRaBS J1522+3144	...
J1536.7–4947	234.197	–49.798	328.261	4.764	0.127	10.7	19.0	0.0	5.7	0.74	0.13	10.3
J1543.1+6130	235.784	61.504	95.383	45.370	0.160	10.5	3.0	1.4	5.4	0.28	0.06	9.5	bzb	CRATES J1542+6129	...
J1553.4+1255	238.368	12.922	23.746	45.225	0.105	23.7	14.5	2.2	17.5	1.08	0.12	18.8	T	...	bzq	RXS J15429+6129 CRATES J1553+1256	...
J1555.8+1110	238.951	11.181	21.911	43.941	0.054	31.5	8.7	2.0	13.1	1.46	0.13	29.3	bzb	PKS 1551+130 CGRaBS J1555+1111	...
J1604.0–4904	241.015	–49.080	332.170	2.541	0.078	11.5	24.3	0.0	7.0	0.96	0.18	10.9
J1615.6–5049	243.914	–50.831	332.354	–0.010	0.233	15.6	46.3	9.6	13.9	2.46	0.34	10.1	†
J1622.4–4945	245.611	–49.765	333.874	–0.009	0.179	16.0	52.4	9.0	13.6	3.25	0.36	11.9	...	1AGL J1624–4946	...	PG 1553+11	...

Table 6—Continued

Name 0FGL	R.A.	Decl.	l	b	θ_{95}	\sqrt{TS}	100 MeV – 1 GeV			1 GeV – 100 GeV			Var.	γ -ray Assoc.	Class	ID or Assoc.	Ref.
							F_{23}	ΔF_{23}	$\sqrt{TS_{23}}$	F_{35}	ΔF_{35}	$\sqrt{TS_{35}}$					
J2001.0+4352	300.272	43.871	79.047	7.124	0.069	13.3	9.5	0.0	6.9	0.78	0.12	12.3	1ES 1959+650	...
J2009.4–4850	302.363	–48.843	350.361	–32.607	0.132	10.9	2.5	0.6	4.3	0.48	0.09	10.5	bzb	CGRaBS J2009–4849 PKS 2005–489	...
J2017.2+0602	304.302	6.048	48.596	–15.991	0.123	12.7	4.2	0.0	4.9	0.56	0.09	12.1	bzu	CLASS J2017+0603	...
J2020.8+3649	305.223	36.830	75.182	0.131	0.060	46.6	73.9	3.9	35.7	6.28	0.32	34.1	...	1AGL J2021+3652	PSR	PSR J2021+3651	14
J2021.5+4026	305.398	40.439	78.230	2.070	0.053	69.6	123.6	5.1	54.8	10.60	0.40	49.7	...	1AGL J2022+4032	PSR	LAT PSR J2021+4044	7
J2025.6–0736	306.415	–7.611	36.883	–24.389	0.077	50.6	40.8	2.0	45.4	2.20	0.17	30.5	T	3EG J2025–0744 1AGL J2026–0732	bzq	CRATES J2025–0735 PKS 2022–07	...
J2027.5+3334	306.882	33.574	73.296	–2.849	0.118	11.2	15.2	0.0	6.7	0.97	0.15	9.3
J2032.2+4122	308.058	41.376	80.161	0.978	0.085	23.9	51.3	4.7	18.1	3.07	0.26	18.8	...	3EG J2033+4118 1AGL J2032+4102	PSR	LAT PSR J2032+4127	7
J2055.5+2540	313.895	25.673	70.660	–12.475	0.130	17.3	5.4	0.8	12.6	0.88	0.11	13.6
J2056.1–4715	314.034	–47.251	352.586	–40.358	0.239	12.5	10.4	1.7	11.9	0.27	0.07	6.5	...	3EG J2055–4716 EGR J2057–4658	bzq	CGRaBS J2056–4714 PKS 2052–47	...
J2110.8+4608	317.702	46.137	88.261	–1.351	0.171	10.7	10.5	3.3	7.0	0.64	0.12	8.0
J2124.7–3358	321.186	–33.981	10.924	–45.441	0.143	14.3	3.5	1.3	6.2	0.67	0.10	13.0	PSR	PSR J2124–3358	4
J2139.4–4238	324.865	–42.642	358.237	–48.332	0.096	20.1	6.9	1.3	12.4	0.79	0.11	16.3	bzb	CRATES J2139–4235 MH 2136–428	...
J2143.2+1741	325.807	17.688	72.016	–26.051	0.215	14.5	11.5	1.7	12.6	0.44	0.08	8.7	bzq	CGRaBS J2143+1743 OX 169	...
J2147.1+0931	326.777	9.519	65.805	–32.236	0.137	19.9	16.0	1.6	19.1	0.55	0.09	12.1	T	...	bzq	CGRaBS J2147+0929 PKS 2144+092	...
J2157.5+3125	329.384	31.431	84.747	–18.258	0.343	10.0	6.9	1.5	8.6	0.38	0.08	7.3	bzq	CGRaBS J2157+3127 B2 2155+31	...
J2158.8–3014	329.704	–30.237	17.711	–52.236	0.064	43.9	16.0	1.4	27.9	2.57	0.18	36.7	T	3EG J2158–3023 EGR J2200–3015	bzb	CGRaBS J2158–3013 PKS 2155–304	15
J2202.4+4217	330.622	42.299	92.569	–10.398	0.160	12.3	7.4	2.0	8.4	0.50	0.09	9.6	...	3EG J2202+4217 EGR J2204+4225	bzb	BZB J2202+4216 BL Lacertae	...
J2203.2+1731	330.815	17.532	75.715	–29.529	0.186	12.7	7.8	1.6	9.6	0.48	0.09	10.2	T	...	bzq	CGRaBS J2203+1725 PKS 2201+171	...
J2207.0–5347	331.765	–53.786	339.948	–49.832	0.223	12.4	10.8	1.8	12.0	0.26	0.07	6.6	T	...	bzq	CGRaBS J2207–5346 PKS 2204–54	...

Table 6—Continued

Name 0FGL	R.A.	Decl.	l	b	θ_{95}	\sqrt{TS}	100 MeV – 1 GeV		1 GeV – 100 GeV		Var.	γ -ray Assoc.	Class	ID or Assoc.	Ref.		
							F_{23}	ΔF_{23}	$\sqrt{TS_{23}}$	F_{35}						ΔF_{35}	$\sqrt{TS_{35}}$
J2214.8+3002	333.705	30.049	86.913	-21.658	0.152	11.9	4.2	0.0	5.4	0.49	0.08	11.2	
J2229.0+6114	337.257	61.240	106.644	2.956	0.076	32.8	44.9	5.4	26.5	2.65	0.21	23.2	...	3EG J2227+6122 EGR J2227+6114 1AGL J2231+6109	PSR	PSR J2229+6114	11
J2229.8-0829	337.452	-8.495	55.326	-51.701	0.185	16.8	11.7	0.4	16.1	0.30	0.07	7.5	bzq	CGRaBS J2229-0832 PHL 5225	...
J2232.4+1141	338.117	11.690	77.372	-38.592	0.183	15.2	10.8	1.3	13.2	0.35	0.07	8.2	...	3EG J2232+1147	bzq	BZQ J2232+1143 CTA 102	...
J2241.7-5239	340.430	-52.651	337.395	-54.907	0.151	11.6	5.0	1.5	8.2	0.34	0.07	9.4
J2254.0+1609	343.502	16.151	86.125	-38.187	0.051	149.1	211.7	4.3	144.4	9.83	0.34	76.8	T	3EG J2254+1601 EGR J2253+1606 1AGL J2254+1602	bzq	CGRaBS J2253+1608 3C 454.3	16
J2302.9+4443	345.746	44.723	103.437	-14.004	0.155	13.6	3.5	1.3	5.8	0.66	0.10	12.3
J2325.3+3959	351.334	39.993	105.532	-19.952	0.118	11.4	0.9	0.3	5.7	0.37	0.07	10.3	T	...	bzb	CRATES J2325+3959 B3 2322+396	...
J2327.3+0947	351.833	9.794	91.159	-47.821	0.218	17.1	15.5	1.6	17.1	0.34	0.07	8.4	T	...	bzq	CGRaBS J2327+0940 PKS 2325+093	...
J2339.8-0530	354.961	-5.512	81.487	-62.474	0.188	13.6	4.9	0.0	5.5	0.55	0.09	12.7
J2345.5-1559	356.389	-15.985	65.677	-71.092	0.239	15.5	9.9	1.3	15.9	0.36	0.08	8.1	T	...	bzq	CGRaBS J2345-1555 PMN J2345-1555	...

References. — 1 (Abdo et al. 2008), "The Fermi Gamma-Ray Space Telescope Discovers the Pulsar in the Young Galactic Supernova Remnant CTA 1", 2 (Abdo et al. 2009e), "Discovery of high-energy gamma-ray emission from the globular cluster 47 Tucanae with *Fermi*", 3 (Abdo et al. 2009o), "Pulsed Gamma-rays from the millisecond pulsar J0030+0451 with the Fermi Large Area Telescope", 4 (Abdo et al. 2009d), "Discovery of a Population of Gamma-ray Millisecond Pulsars with the Fermi Large Area Telescope", 5 (Abdo et al. 2009j), "Fermi LAT Observations of LS I +61 303", 6 (Abdo et al. 2009h), "Fermi Discovery of gamma-ray emission from NGC1275", 7 (Abdo et al. 2009p), "Sixteen Gamma-Ray Pulsars Discovered in Blind Frequency Searches Using the Fermi LAT", 8 (Abdo et al. 2009b), "*Fermi* LAT Observations of the Vela Pulsar", 9 (Abdo et al. 2009k), "The peculiar quasar PMN J0948+0022", 10 (Abdo et al. 2009f), "Discovery of pulsed gamma-rays from the young radio pulsar PSR J1028-5819 with the Fermi Large Area Telescope", 11 (Abdo et al. 2009i), "Fermi LAT detection of pulsed gamma-rays from the Vela-like pulsars PSR J1048-5832 and PSR J2229+6114", 12 (Abdo et al. 2009l), "Fermi/LAT discovery of gamma-ray emission from the flat-spectrum radio quasar PKS 1454-354", 13 (Abdo et al. 2009m), "PKS 1502+106: a new and distant gamma-ray blazar in outburst discovered by the Fermi Large Area Telescope", 14 (Abdo et al. 2009n), "Pulsed gamma-rays from PSR J2021+3651 with the Fermi Large Area Telescope", 15 (Aharonian et al. 2009), "Resolving the blazar high-energy spectrum of PKS 2155-304 with HESS and FERMI", 16 (Abdo et al. 2009g), "Early Fermi Gamma-ray Space Telescope

observations of the blazar 3C 454.3”

Note. — Flux units $10^{-8} \text{ cm}^{-2} \text{ s}^{-1}$

Note. — † - possible SNR or PWN association. See Table 2.

Note. — A “0” in the ΔF_{23} column indicates that the entry in the F_{23} flux column is a $2\text{-}\sigma$ upper limit.